Predictive modeling and optimization-based control of particulate polysilicon reactor systems for enhanced solar cell production

by

Carlos Eduardo Veloz Marmolejo

B.S., Yachay Tech University, Ecuador, 2021

A THESIS

submitted in partial fulfillment of the
requirements for the degree

MASTER OF SCIENCE

Tim Taylor Department of Chemical Engineering
Carl R. Ice College of Engineering

KANSAS STATE UNIVERSITY
Manhattan, Kansas

2024

Approved by:

Major Professor
Dr. Davood B. Pourkargar

Copyright

Abstract

Solar-grade silicon production has a pivotal role in the photovoltaic industry, especially in the manufacturing of solar panels. It represents approximately 20% of the total solar cell manufacturing cost. Consequently, reducing the production cost of solar-grade silicon is a primary factor in enhancing the solar manufacturing process. In particular, fluidized-bed reactors (FBR) for silane pyrolysis appear as a promising technology for solar-grade silicon production, representing a more energy-efficient process with more operational benefits than conventional technologies. However, controlling the FBR system is a challenging task due to the complex gas-solid interactions. Limited research has been conducted on developing control strategies for enhancing silicon production in FBR systems. This work develops a predictive modeling framework for silicon production in FBRs that can be used for real-time optimization and control purposes. The proposed model characterizes the particle size distribution of the product and the powder loss. Two different flow regime modeling approaches are considered to describe the silane pyrolysis reaction and characterize the deposition rate that contributes to particle growth. A discrete population balance equation is used to estimate the particle size distribution as a function of the deposition rate. The proposed model is compared against comprehensive models reported in the literature, showing satisfactory results. A nonlinear model predictive control is then utilized to regulate the system at the desired operating conditions. Detailed open-loop and closed-loop simulation studies demonstrate the successful integration of nonlinear MPC and the proposed predictive modeling approach.

Table of Contents

List of Figures

List of Tables

Chapter 1

Introduction

In 2022, the global photovoltaic industry reached the terawatt era, with a cumulative installed capacity of 1.185 GW[7]. Crystal silicon cells represent more than 95% of this capacity[8]. Solar-grade silicon, a high-purity polysilicon, is an essential component in the photovoltaic supply chain, representing approximately 20% of the total solar cell manufacturing cost. Consequently, reducing the production cost of solar-grade silicon is a crucial factor in this industry[9]. The fluidized bed reactor (FBR) for silane pyrolysis represents a promising approach to achieve cost reduction, compared to the conventional Siemens process[3]. FBR systems are more energy-efficient and provide higher operational benefits, which make them a more efficient platform for solar-grade silicon production. The production efficiency using this technology has been supported by various experiments and computational studies[10]. Previous research studies have established reaction mechanisms and developed reaction rate expressions for silane pyrolysis in fluidized bed reactors[11;12].

Furthermore, several studies have been aligned to evaluate the FBR's performance and fine-tune its operation for efficient production of solar-grade silicon[13–16]. The dynamics involved in polysilicon production in FBR systems are characterized by the production scale, growth rate, and the co-presence of a dispersed phase within a continuous phase. These processes involve complex physico-chemical phenomena, including particle nucleation, coagulation, growth, and breakage, as the two phases coexist, influencing the spatial distribution of properties such as size, shape, molecular weight, and porosity[17].

In the particulate process, the distribution of properties occurs across both external (space and time) and internal (particle size) coordinates[18]. The population balance equation (PBE) governs the evolution of these properties along the external coordinates. However, when combined with the mass balance equation of the continuous phase, it results in a set of partial integro-differential equations that are challenging to solve. Several numerical methods have been developed for solving this set of equations, including moment transformation[19], discretization approaches[20], orthogonal collocation[21], and method of weighted residuals[18]. Discretization methods have been proposed for predicting particulate systems such as crystallization and emulsion polymerization[22–24]. White et al.[20] presented a particulate phase model combining mass and population balances over discrete intervals of particle sizes. The proposed model was applied to produce solar-grade silicon, demonstrating a reduced computational time compared to other existing methods. Controlling FBR systems involves challenges due to the complex gas-solid interactions involved in the process. Several modeling approaches have been developed to address these issues. Two models for silane pyrolysis in FBR systems have been initially proposed[11]: one employing an ideal well-mixed reactor (CSTR) to capture the fluidized reactor's behavior under specific conditions, and the other based on more comprehensive fluidized-bubbling bed model[25], which better represents the system physics. The model predictions for silane pyrolysis in FBR systems have been compared against experimental data[26]. A numerical model for reactions in the fluidized bed grid zone for chemical vapor deposition of polycrystalline silicon was also proposed[27]. These studies present detailed insights into the silane decomposition reaction mechanisms and diverse modeling approaches for FBR systems. However, some models are limited to monodisperse distributions of seed particles that grow at the same rate. A comprehensive multiphase gas-solid dynamic model that incorporates the population balance equation, hydrodynamics, and silane decomposition rate was developed to predict the batch growth of a monodisperse distribution of silicon particles in a submerged spouted bed reactor[28]. Despite these advances in several modeling approaches, few studies have focused on devising control strategies for silane pyrolysis in FBR systems. White et al.[20] proposed a simplified model that can be easily tuned using experimental data, facilitating control purposes. This model incorporates feedback control theory into steady-state simulations to regulate the mass hold-up in the reactor and average product size.

Several multiphase gas-solid simulation studies have used computational fluid dynamics tools to analyze FBR system dynamics and enhance model reliability. These studies have contributed to developing multi-scale modeling approaches integrating data like void fraction, drop pressure, and temperature profiles into deterministic models. Prior research has primarily used traditional control strategies due to the complexity of the models[29–31]. While other works have demonstrated the feasibility of more advanced control approaches[3;24;32]. Du et al.[33] proposed a multi-scale model framework for silicon production in FBR systems, which could be integrated with a control system. Nevertheless, these studies have solely discussed control strategies for regulating mass hold-up and particle size distribution, overlooking the objective of minimizing powder loss to enhance process yield. Advanced control strategies, such as model predictive control (MPC), appear promising in addressing this challenge.

This study is focused on developing a predictive modeling framework for particulate polysilicon reactor systems for process control and real-time decision-making applications. Reduced-order models are proposed for ideal and non-ideal mixed-flow conditions. These models are then employed as the basis for MPC designs, aiming to precisely regulate particle size distributions and minimize powder loss. The ultimate goal is to enhance the operational efficiency of FBR systems and concurrently reduce production costs associated with solar-grade silicon. The developed reduced-order models encompass a comprehensive integration of reaction mechanisms, population balance, and mass balances for the various components involved in the reaction medium to predict the silane decomposition and particle growth.

Several simulations are performed to evaluate the performance of MPC incorporated with the proposed model.

Chapter 2

Photovoltaic Manufacturing Process

Silicon-based modules are the dominant technology in the photovoltaic industry, accounting for 95% of the installed capacity[8]. The purity of silicon used in the manufacturing process is a pivotal factor in ensuring the efficiency of the solar cells. The supply chain of the photovoltaic industry is shown in Fig 2.1

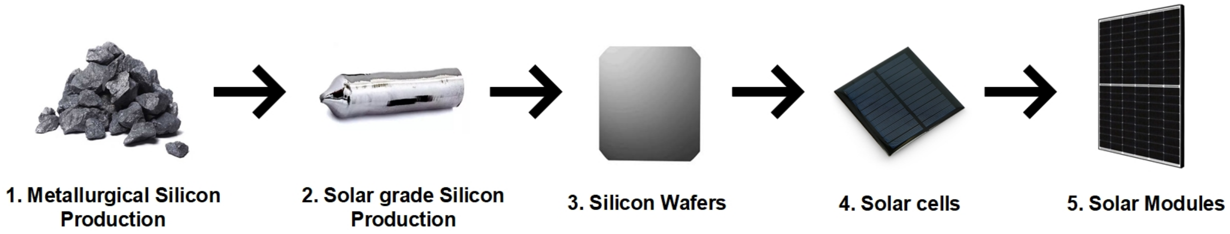

Figure 2.1: *Silicon photovoltaic manufacturing process*

The manufacturing process starts with producing metallurgical-grade silicon (Mg-Si) with the carbothermic reduction of silicates in electric furnaces[34]. In this initial step, large amounts of energy are used to break the silicon-oxygen bonds in the silicates (SiO_2) via endothermic reaction with carbon to produce metallurgic grade silicon, achieving around 98.5% level of purity[35]. Then, this metallurgical grade silicon is refined to obtain polycrystalline silicon, which is high-purity silicon (99.9999999%), often called 9Ns or solar-grade silicon (Sg-Si). Generally, this step is performed via chemical conversion of the metallurgical silicon to gaseous Si-based compounds and vapor deposition of these gaseous species onto solid silicon rods. Subsequently, these silicon rods are melted and recrystallized to produce monocrystalline or polycrystalline silicon wafers, depending on the requirements of the selected process. These silicon wafers are chemically doped, coated, and treated to make the solar cells. Finally, these solar cells are assembled into panels integrated with micro-electronic components and frameworks established by the photovoltaic companies to elaborate the solar modules.

Producing solar-grade silicon from metallurgic-grade silicon involves a high energy consumption and capital-intensive process with limited yield[10]. Solar-grade silicon is a critical material in the photovoltaic supply chain, and it represents approximately 20% of the total solar cell production cost[35]. Therefore, several improvements and technologies have been developed to enhance polysilicon production and minimize the production costs associated with solar-grade feedstock.

2.1 Solar-grade Silicon Production

Solar-grade silicon or polysilicon requires the conversion of Mg-Si to intermediate gaseous Si species, which are purified and then reduced or thermally decomposed into high-purity silicon[34;35]. Hence, several technologies have been explored based on the intermediate gaseous Si compounds employed in polysilicon production. Fig 2.2 provides an overview of the conventional process and the technology under development.

The silicon production is primarily based on the chemical vapor deposition (CVD) process. A variety of gases and compounds have been tested for silicon production, but monosilane SiH_4 (silane) and trichlorosilane $SiHCl_3$ (TCS) are the most frequently employed[36]. In particular, the Siemens process is still the mainstream of solar-grade silicon production. It represents around 90% of the global polysilicon production[4].

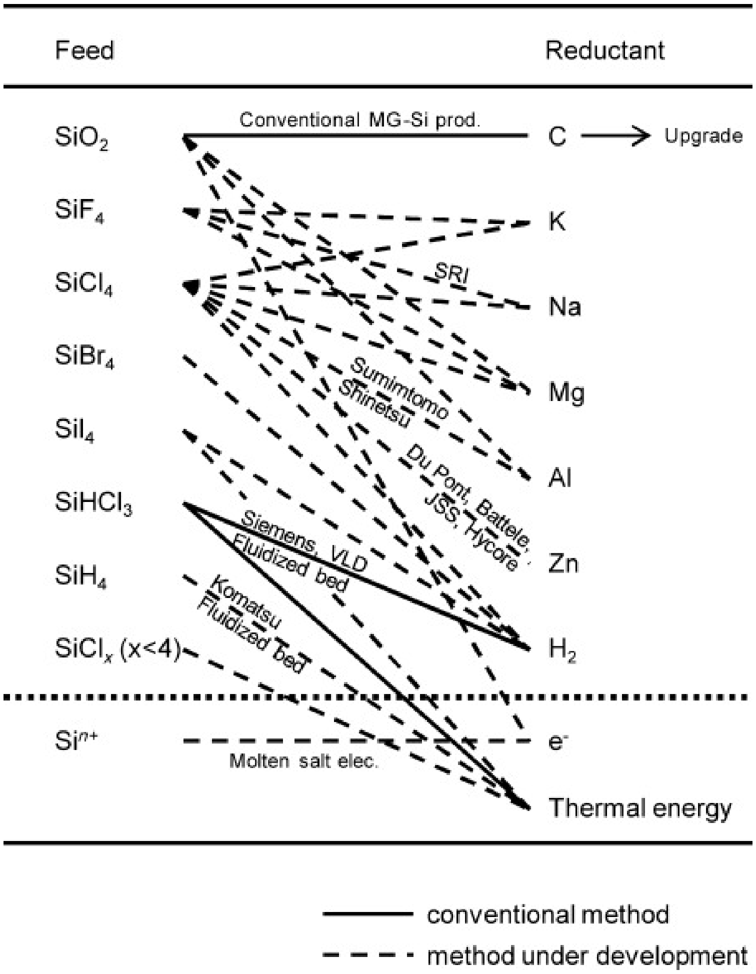

Figure 2.2: *Reaction pathways for solar-grade silicon production using intermediate Si-based compounds*[1]

2.2 Siemens Process

The Siemens process mainly involves the production of trichlorosilane ($SiHCl_3$ or TCS) as an intermediate species. In general, the Siemens process can be divided into four key steps: the production of TCS from metallurgic-grade silicon, the purification of TCS, the thermal decomposition or reduction of TCS into solid polysilicon, and the recycling of byproducts and recovery of remaining TCS[10].

The first step is the hydrochlorination of the metallurgic grade in a fluidized bed reactor to produce trichlorosilane (TCS) at a temperature within the range of 300 to 350°C:

$$\mathrm{Si\,(s) + 3\,HCl\,(g) \longrightarrow SiHCl_3(g) + H_2(g)}$$

This reaction implies several reaction mechanisms and possible side reactions. However, around 90% of the overall yield is converted into TCS[10]. The generated TCS gas is purified through multiple distillation columns to remove most of the impurities generated by the side reactions. The purified TCS is fed into a jar bell-shaped reactor containing heated seed silicon rods. Fig 2.3 illustrates a schematic description of the bell-shaped reactor used in this process. The rods are heated by electrical resistance to a temperature between 1100-1150°C, which is the temperature where the TCS starts to decompose into solid Si and deposits on the silicon rods:

$$2\,\mathrm{HSiCl_3(g)} \longrightarrow \mathrm{Si\,(s)} + 2\,\mathrm{HCl\,(g)} + \mathrm{SiCl_4(g)}$$

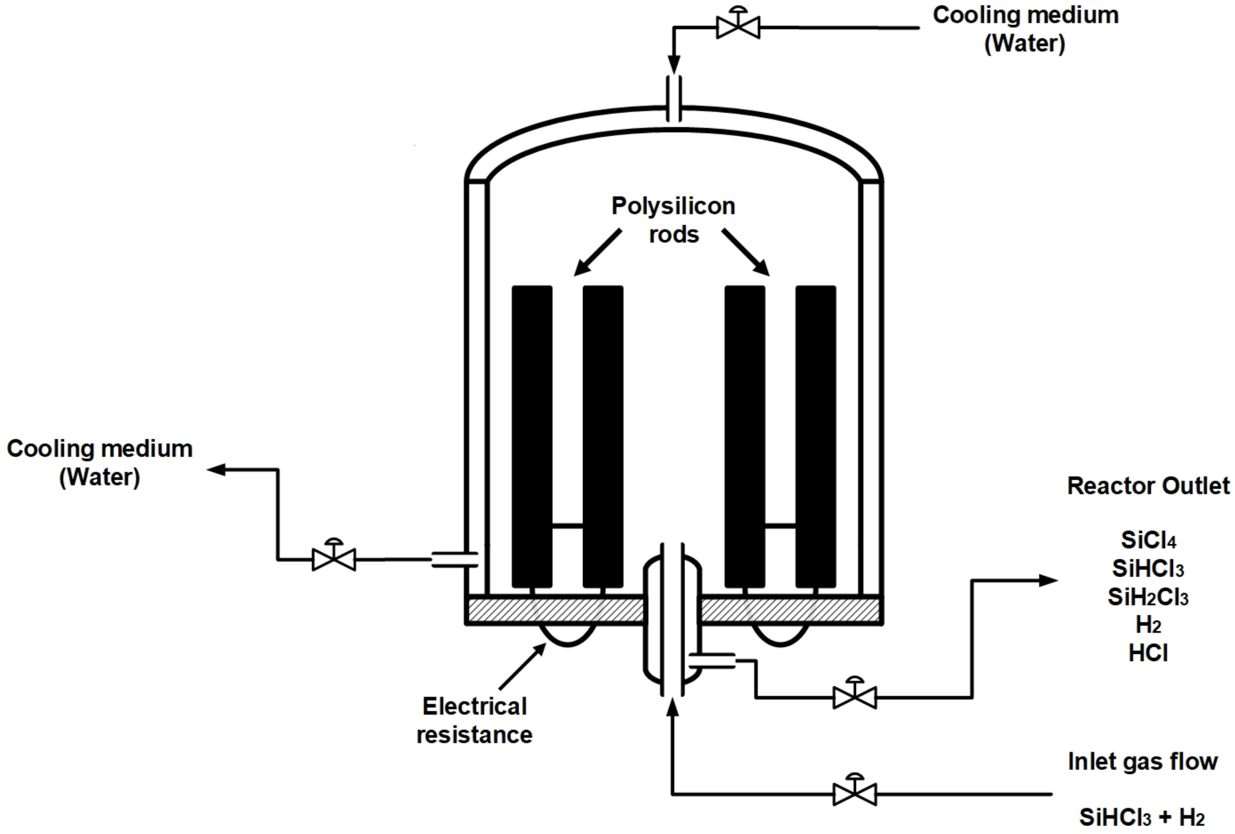

Figure 2.3: *Jar bell reactor used in Siemens process.*

Silicon deposits onto the rods via a chemical vapor deposition process. The seed Si rods increase in diameter to the desired size and are removed from the reactor. It is also necessary to maintain a significant temperature difference between the surface for deposition and the reactor wall to increase the yield of the overall process[37]. TCS is either thermally decomposed or reduced by hydrogen (both can co-occur[38]) to produce Si with other byproducts such as HCl, SiH_2Cl_2, $SiCl_4$,$SiCl_2$ and H_2[10;39]. These remaining gases are recovered and separated through distillation. The recovered H_2 and TCS are fed back into the bell jar reactor, while the $SiCl_4$ needs to be eliminated and can be utilized to produce SiO_2, which is further used in the manufacture of metallurgic grade silicon[4].

The modified Siemens process has been developed to increase efficiency and economic benefit. It combines the generated $SiCl_4$ with H_2 and metallurgic-grade silicon to produce TCS during the hydrochlorination step[40]:

$$\mathrm{Si\,(s) + 3\,SiCl_4(g) + H_2(g) \longrightarrow 4\,SiHCl_3(g) + HCl\,(g)}$$

Hence, the modified Siemens process utilizes the generated $SiCl_4$ and reduces the amount of HCl in hydrochlorination process. However, this modification requires that hydrochlorination occur at higher temperatures between 500-600°C[10]. Despite the Siemens process being the dominant technology for polysilicon production, it presents considerable performance limitations. The slow deposition rate and the batch nature of the process are some critical limitations. Furthermore, the large amount of input energy and the thermal losses involved in the system result in an energetically inefficient process[41]. Moreover, the byproducts generated during the process need posterior treatment due to the chlorine content, which could create corrosion issues in the equipment and pipelines.

2.3 Fluidized Bed Reactor

The silane (SiH_4) decomposition represents the second most widely used commercial process for silicon production[39]. The fluidized-bed technology using silane represents a promising alternative to the Siemens reactor because it provides operational benefits such as continuous operation and excellent heat and mass transfer characteristics. A schematic representation of the fluidized bed reactor utilized in polysilicon production is illustrated in Fig 2.4. A solid bed of seed silicon particles is preloaded to promote the chemical vapor deposition of silicon. A mixture of silane and hydrogen is fed at the bottom of the reactor to achieve the fluidization of the silicon particles. The solid bed is heated to reach the reaction temperature to thermally decompose the silane into solid silicon and hydrogen gas. The overall pyrolysis reaction governs the silane decomposition in FBR systems:

$$\mathrm{SiH_4(g)} \longrightarrow \mathrm{Si\,(s)} + 2\,\mathrm{H_2(g)}$$

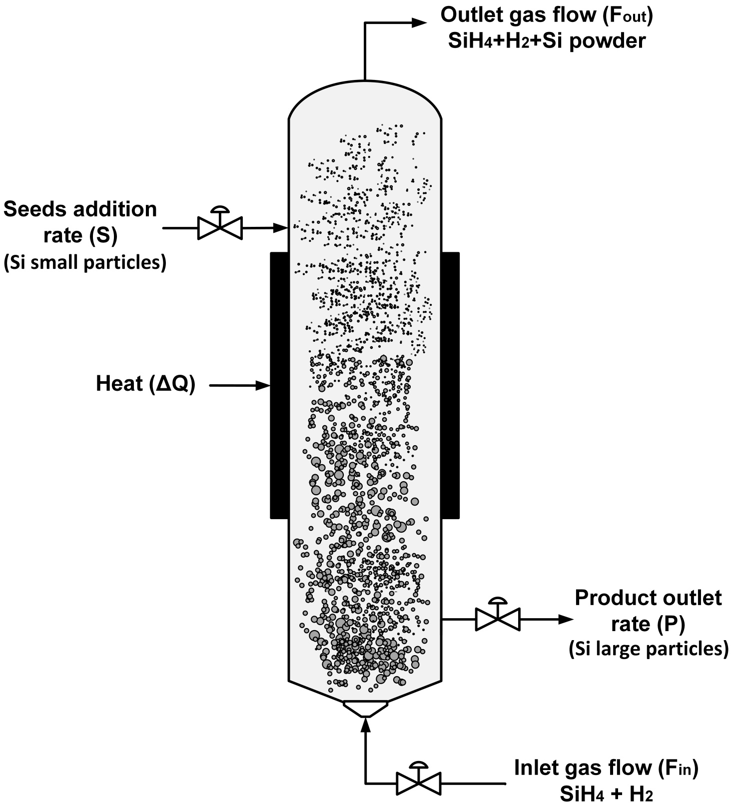

Figure 2.4: *Fluidized bed reactor.*

The reaction is fast and complete if the reaction temperature is above 650°C. The solid silicon deposits onto the surface of the Si seed particles, producing the growth of the particles. The reaction mechanism of silane pyrolysis involves a complex set of elementary steps and side-reactions, and there is no agreement in the literature to the exact mechanisms[4;10;11]. However, silane pyrolysis is usually divided into two primary reactions: heterogeneous and homogeneous decomposition. The heterogeneous decomposition occurs on the surface of the seed particles, where silicon deposits on the surface of solid silicon as a crystalline solid via chemical vapor deposition. Homogenous decomposition takes place away from the particle surface, forming a gaseous precursor that can nucleate and generate amorphous brown powder. This powder is usually referred to as fines and is considered undesirable during the operation. This powder can be scavenged by existing silicon particles and subsequently recrystallized to contribute to the particle growth[42]. However, it could also cause fouling and unwanted deposition issues on the reactor wall. The unscavenged fines are exhausted in the gas phase, with the unreacted silane and hydrogen at the top exit, reducing the overall yield. As the silicon particles grow in the reactor, the large particles are removed from the bottom as the final product. In addition, new seed particles are incorporated to ensure the mass hold-up and constant average particle size.

2.4 Comparison of Siemens Process and Fluidized Bed Reactor Process

Each technology has operational benefits and limitations for the production of polysilicon. The Siemens process is a mature technology in the photovoltaic industry, and several attempts to increase its efficiency have been explored[1;43]. However, with the increasing demand for polysilicon production, the FBR technology represents a promising alternative to achieve a significant cost reduction[36]. Table 2.1 summarizes and compares several relevant features between these technologies.

There are several features and significant differences between these two technologies. The FRB system provides operational benefits such as continuous operation and lower energy consumption. In contrast, the Siemens process is a batch process that implies extensive time and effort to remove the product and set up the system for an operation cycle. Furthermore, the production of silicon using an FBR system requires 80-90% less electrical energy than

Table 2.1: *Comparison of several factors between Siemens reactors and fluidized-bed reactors in the production of polysilicon*[6]

Criteria	**Fluidized-bed process**	**Siemens process**
Potential for reduced Si cost	Potential for reduced Si cost	Limited future cost reduction likely
Operational mode	Continuous operation	Batch process
Product characteristics	Flowable, spherical Si product	Crushing step required to convert rods to chunk Si
Feed gas	Noncorrosive feed gas	Corrosive feed gas
Reaction completion	Reaction goes to completion	Limited equilibrium reaction producing HCl and SiCl4
Powder production	Produces higher amounts of powder	Minimal Si powder produced
Energy requirements	80–90% less energy required	High electric power consumption
Cooling requirements	Minimal cooling required (hot wall)	Large cooling load to cool reactor walls (cold wall)
Technology status	Developing technology	Mature optimized technology
Operating temperature	Reactor operates at 650–850 C	High temperature reactor operates near 1150 C
By-product	Chloride-free feed product	Residual chloride in product from HSiCl3 feed
Reactor environment	Violent fluidized-bed environment	Stable, fixed reactor environment

the Siemens process, significantly reducing the production cost. The feed gas used in each process is also significantly different. In FBR systems, silane pyrolisis can be carried out at lower temperatures than TCS decomposition in the Siemens process. In addition, higher deposition rates are obtained via silane pyrolysis in fluidized-bed systems[10]. The presence of chlorine compounds in the process could lead to operational problems. For instance, the chlorine content in the byproducts and feed gas used in the Siemens process can lead to corrosion issues in the equipment and pipelines.

On the other hand, the main drawback of using silane as a feed gas is that a disproportionation plant is required to produce silane from trichlorosilane[6]. The final product characteristics are also significant factors for the downstream manufacturing process. In particular, the spherical silicon particles are favored for handling the polysilicon in the subsequent crystallization processing. In contrast, the polysilicon rods produced in the Siemens process must be crushed into smaller particles to feed into the downstream processing. Furthermore, the spherical granular product from a fluidized bed reactor is uniquely suited as feed for continuous crystal pullers in manufacturing monocrystalline silicon[44]. The continuous flow between subsequent process units is a cost-reducing factor that could be enhanced with the FBR technology.

Solar cell efficiency highly depends on the purity of the silicon used in manufacturing. Hence, despite the operational limitations, the Siemens process remains dominant due to the high purity that can be obtained in the final product. FBR technology usually does not reach the same purity levels as the Siemens process due to the significant inhomogeneity associated with higher deposition rates[45]. Nevertheless, it can reach acceptable purity levels by employing suitable temperature control and achieving a low amount of powder formation[46]. Powder formation is one of the major deficiencies of FBR technology. It reduces the overall yield and produces undesired deposition on the reactor wall. The fines formation cannot be completely suppressed during operation, and a significant fraction of this powder is exhausted in the gas phase. Hence, minimizing the powder loss is crucial to establishing the FBR system as a commercially viable process for polysilicon production. Several techniques and operational conditions have been studied to reduce powder formation. Increasing the residence time of the gas phase by reducing the average particle size and the feed gas flow rate to increase the time for the silane gas to react onto the available surface provided by the seed particles[6]. This reduction in the average particle size increases the available surface area to promote the heterogeneous decomposition of silane onto the seed particles. This reduction is obtained by adding new Si seed particles to the system, which also produces that powder is more likely to be scavenged by the larger Si particles.

In contrast, reducing the feed gas flow rate causes a significant reduction in the deposition rate due to less silane available to react in the system. In addition, regulating the SiH_4/H_2 mole ratio of the feed gas is an alternative to reducing the powder formation in actual operation. The optimal feed gas concentration is within the range of 10-30% of silane in hydrogen depending on the reactor geometry and operational conditions[36]. The hydrogen works as carry gas and dilutes the concentration of silane, reducing the reaction rate and, consequently, the powder formation. On the other hand, injecting HCl into the FBR system also contributes to reducing the formation of the fines due to HCl reacting with the silicon particles to produce TCS and eliminates silicon powder as observed in the Siemens process operation[47].

FBR systems exhibit higher operational efficiencies and are more energetically efficient, making them a more efficient platform for solar-grade silicon production. However, the Siemens process is still the dominant technology due to the challenges and limitations of silane-based FBR operation. The fluidized-bed technology remains under development, and its theoretical potential has not been reached. Hence, optimizing the operation of FBR technology is necessary to establish it as a viable commercial alternative for more cost-effective polysilicon production. Hence, analyzing the effect of several factors, such as temperature, void fraction, pressure, flow rates, and particle size, is essential. Therefore, developing reliable models can provide helpful information to comprehend the effects of different factors on the underlying system physics.

2.5 Modeling Approaches for Fluidized Bed Reactors

Developing comprehensive and reliable models for fluidized reactors is challenging due to the intricate nature of gas-solid interactions. Filtvedt et al.[36] provided a detailed review of FBR modeling approaches and scale-up considerations. Furthermore, this work analyzes the deposition mechanisms, fines formations, and how microscale effects can be incorporated into the model development. In literature, two main classes of modeling approaches have been used to describe the behavior of FBR systems. The first model category relies on phenomenological-based models employing deterministic and analytical relationships for studying chemical reactions in the fluidization process. Prior research has investigated some variations of two-phase models[11] and bubbling-bed models[25] to describe the silane-based FBR system. However, due to the complex physicochemical phenomena involved in the FBR operation, these modeling efforts cannot accurately capture the reactor's dynamics using analytical solutions. The second model type is based on computational fluid dynamic (CFD) models to solve each phase's mass, momentum, and energy equations with phase interaction terms and constitutive relationships[6;10]. Euler-Euler models and discrete element method-type models are the most representative modeling approaches in this category. These models provide a high-resolution and comprehensive description of the physical phenomena inherent in the FBR system. However, the high computational cost causes these models cannot be solved in real-time for process control purposes. As a result, more recent research has focused on developing multiscale modeling frameworks to combine the benefits of both modeling categories. This modeling procedure aims to represent the system using two or more submodules that describe the phenomena at different scales[3]. Each submodule represents a partial model that describes the phenomena at different time or length scales. These interconnected modules share information, which attempts to create a flexible modeling framework by linking two or more modules. This modeling technique is beneficial for systems that uni-scale models cannot represent due to the different scales involved in the system dynamics[48]. Despite accurate modeling and flexibility benefits, integrating and pairing the scales between submodules is challenging. A brief review of the modeling approaches considered for representing silane-based FBR systems is presented in the following sections.

2.5.1 Fludized Bed Reactor Fundaments

An understanding of the fluid dynamics during the fluidization process is essential to study FBR systems. Therefore, describing the phenomena and fluid mechanics is necessary to develop reliable models for fluidized bed reactors. The hydrodynamics of a fluidized bed are determined essentially by the balance of forces between particles and gas velocity[49]. It is possible to set the fluidization regime by controlling the gas velocity. Fig 2.5 illustrates the hydrodynamic behavior of the fluidized-bed system at different gas velocities.

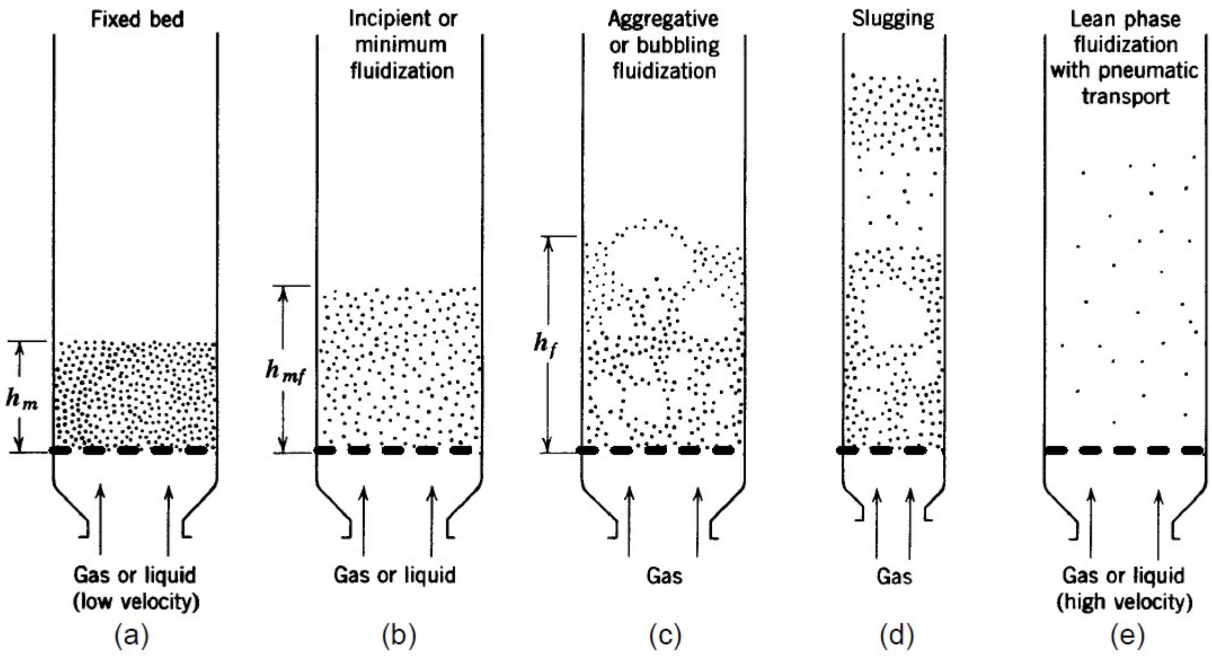

Figure 2.5: *Hydrodynamic behaviour of fluidized bed*[2]

The solid bed is supported by a perforated or porous distributor plate, while the gas flows upwards through this bed. The distributor has a significant effect on the flow pattern and bubble formation. The fixed bed regime is characterized by a low gas velocity, maintaining the bed static (Fig 2.5a). Then, as the gas velocity increases until a specific value, the total drag on the particles will equal the weight of the bed, and the particles will start to lift, increasing the porosity and barely fluidizing (Fig 2.5b). This situation corresponds to the minimum fluidization regime, which is the starting point of the fluidization regime. The bubbling regime arises when the gas velocity exceeds the minimum fluidization value (Fig 2.5(c)), leading to an increase in the expansion and void fraction of the solid bed. This increment in the gas velocity generates instabilities in the flow, and the gas starts to bypass the bed in the form of bubbles[50]. The difference between the velocity at which the bed begins to expand and when the bubbles appear is very small and sometimes nonexistent[2]. A further increase in the gas velocity will lead to a slug flow regime (Fig 2.5(d)), which is a chaotic and unstable operation of the fluidized bed. At extremely high velocities, the particles are transported out of the reactor by a pneumatic transport regime, ideal for circulating fluidized beds[2;51]. The relationship between the gas velocity and the fluidization regime described previously is displayed in Fig 2.6.

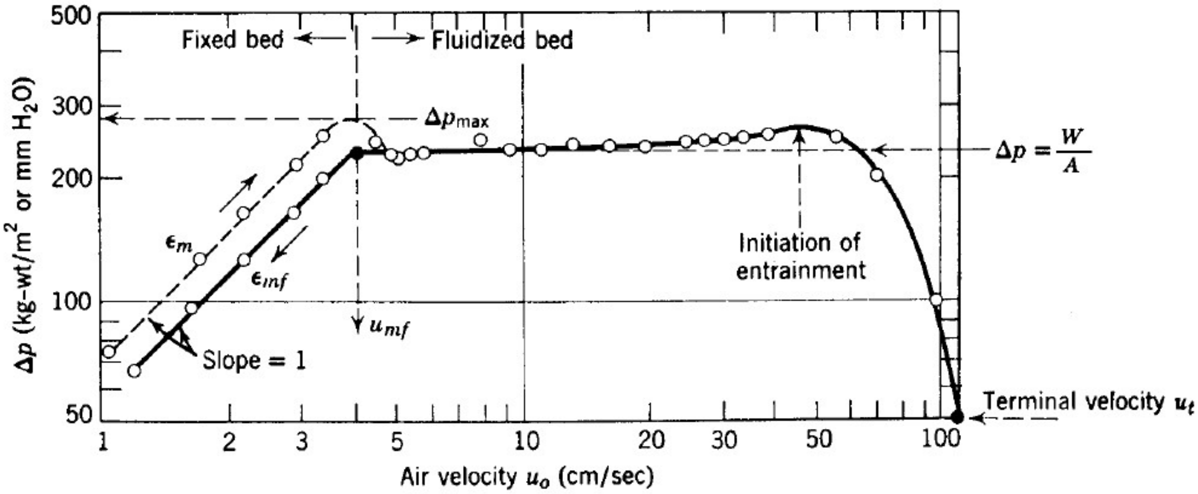

Figure 2.6: *Gas velocity vs Drop pressure diagram*[2]

The bed's fluidization can also be characterized by the relationship between the gas velocity (u_o) and the pressure drop (ΔP). When the gas flows through the solid bed, it experiences a drop in pressure due to the bed expansion. The region covered by $1 \leq u_o \leq 4\ cm/s$ corresponds to the fixed bed regime, where the pressure drop increases linearly with increasing gas velocity. This section can be described by the Ergun equation. The pressure drop keeps growing until the total drag on the particles equals the weight of the bed, and the particles will start to fluidize. This equilibrium point is characterized by the minimum fluidization velocity (u_{mf}), and the pressure drop will not increase with an increase in velocity beyond this point. The region $4 \leq u_o \leq 50\ cm/s$ where the pressure drop remains constant is defined as the bubbling region. Finally, the pressure drop decreases when the gas velocity is above the terminal velocity (u_t), and it is when the pneumatic transport occurs. The physical properties and characteristics of the particles have a significant influence on the fluidization behavior. Geldart[52] categorized the fluidization behavior based on the particle's characteristics:

- Group A: The particles are easily fluidized. They has a smooth and homogeneous fluidization behaviour after achieve the minimun fluidization condition.In general, they are small particles ($30 \leq d_p \leq 150 \mu m$) with low density ($\leq 1.4 g/cm^2$).

- Group B: The particles fluidize well for relatively high gas flow velocities. The formation of bubbles appears at the beginning of the fluidization (i.e., minimum fluidization velocity) and tends to grow. They are particles with a medium size ($40 \leq d_p \leq 500 \mu m$) and the density within ($1.4 - 4 g/cm^2$.

- Group C: They are very small particles ($d_p \leq 40 \mu m$) and cohesive, making fluidization difficult due to the interparticle forces, and the particles are prone to form clusters or agglomerations.

- Group D: They are dense and large particles ($d_p > 500 \mu m$). Fluidization is difficult and non-uniform. For this type of particle, a stable spouted bed can be ideally formed.

The average seed silicon particle used in the FBR system for polysilicon production is Group B of the Geldart[52]'s classification[39]. In particular, the physical properties determine the minimum fluidization condition, essential for modeling fluidized-bed systems[4;52]. The minimum fluidization velocity can be determined by the Ergun equation:

$$\begin{gathered} u_{mf} = \left(\frac{\phi d_p \eta}{150\mu}\right)^2 \frac{\epsilon_{mf}^3}{1-\epsilon_{mf}} \\ \eta = g(\rho_c - \rho_g) \end{gathered} \tag{2.1}$$

where ϵ_{mf} is the void fraction at minimum fluidization condition, ϕ is the sphericity or shape factor of the particles, ρ_p is the particle density, ρ_g is the gas density, d_p is the particle diameter, μ is the viscosity of the gas and g corresponds to the gravity. The void fraction at minimum fluidization condition is given by[2]:

$$\epsilon_{mf} = 0.586 \phi^{-0.72} \left(\frac{\mu^2}{\rho_g \eta d_p^3}\right)^{0.029} \left(\frac{\rho_g}{\rho_c}\right)^{0.021} \tag{2.2}$$

Considering factors such as the pressure drop, bed porosity and gas velocity is also necessary to estimate essential parameters such a bubble diameter and velocity, which have a significant influence in the mass and heat transfer between the gas phase and the solid phase[25]. Several correlations have been proposed in the literature to determine these parameters[2;4].

2.5.2 Phenomenological based models

Several modeling attempts using deterministic models have been explored to describe the dynamic behavior of FBR systems for silane pyrolysis. Praturi et al.[53] proposed an early model deriving kinetic rate expression for 8 elementary reaction steps, including mass transport of silane, hydrogen, homogenous and heterogenous decomposition of silane, homogenous nucleation of silicon, heterogenous nuclear of silicon, and silicon crystal growth. Nevertheless, these expressions were limited due to the lack of experimental data to achieve a complete understanding of the reaction mechanism pathways. Then, Lai et al.[11] presented both an ideal well-mixed reactor (CSTR) model and a two-phase bubbling fluidized-bed model[25] to describe the FBR system. This work also includes a population balance model to predict the concentration and growth of the silicon fines generated by the homogenous decomposition. These models were compared against experiments, showing that the two-phase model achieved better agreement with the experimental data. The ideal well-mixed model established an upper limit of silicon production by overestimating the deposition rate, while the fluidized-bed bubbling reactor (FBBR) model overpredicts the formation of fines. They also concluded that ensuring an excellent gas-solid contact reduces the formation of the fine during operation.

The two-phase model assumes that the FBR is divided into emulsion and bubble phases, where mass and heat transfer are exchanged between these adjacent phases. The bubble phase contains a minimal amount of solids, while the emulsion phase contains most of the solids of the bed. The bubbles are not spherical; they have a hemispherical top and a pushedin bottom. Each gas bubble has a wake that contains a significant amount of solids, and while it rises, it pulls up the wake with its solids behind it[25]. Small bubbles are formed near the plate distributor at the bottom and grow while rising along the reactor. The initial bubble diameter (d_{b0}) size formed at the surface of a perforated and porous gas distributor plate is given by the following expressions:

- Perforated plate distributor

$$d_{b0} = 0.347 \left[A_c \left(\frac{u_0 - u_{mf}}{N_d} \right) \right]^{2/5} \tag{2.3}$$

or

$$d_{b0} = \frac{1.3}{g^{0.2}} \left(\frac{u_0 - u_{mf}}{N_{or}} \right)^{2/5} \tag{2.4}$$

- Porous plate distributor

$$d_{b0} = 0.00376 \left(\mu_0 - \mu_{mf} \right)^2 \tag{2.5}$$

while the maximum bubble diameter d_{bm} is given by:

$$d_{bm} = 0.652 \left[A_t \left(u_0 - u_{mf} \right)) \right]^{2/5} \tag{2.6}$$

where u_{mf} is the minimum fluidization velocity of the bed, is the gravity term, u_0 is the superficial gas velocity, A_c is the cross-sectional area of the reactor, and N_{or} is the number of orifices in the distributor. The relationship of the bubble diameter as a function of the reactor height (h) can be defined by the following expression[6]:

$$d_b = 0.0085 \left[1 + 27 \left(u_0 - u_{mf} \right)^{1/3} \right] (1 + 6.8h)^{1.2} \tag{2.7}$$

Furthermore, Mori and Wen[54] also developed an expression using data from several studies covering bed diameters from 7 to 130 cm, minimum fluidization velocities of 0.5 to

20 cm/s, solid particle size within the range between 0.006 to 0.045 cm.

$$\frac{d_{bm}-d_h}{d_{bm}-d_{b0}}=e^{-0.3\frac{h}{D_t}} \tag{2.8}$$

Where d_b is the bubble diameter at a specific distance h in the reactor of diameter D_t. In addition, a correlation based on a statistical coalescence model is also reported in the literature[2]:

$$d_b=0.853\left(\sqrt[3]{1+0.272\frac{u_0-u_{ms}}{cm/s}}\right)\left[1-0.0684\left(\frac{h}{cm}\right)^{1.21}\right] \tag{2.9}$$

The bubble size predicted by this equation is similar to the predicted values by the previous expression for larger and smaller diameter beds studied by Mori and Wen[54].On the other hand, the rise velocity of the bubbles (U_{rb}) and the fraction occupied by bubbles (δ) are given by[2]:

$$U_{br}=0.71\sqrt{gd_b}+u_0-u_{mf}. \tag{2.10}$$

$$\delta=\frac{u_0-u_{mf}}{u_b} \tag{2.11}$$

These parameters are essential to establish the fluidized-bed system's mass and energy balance between the two phases. Several derivations have been developed based on the two-phase assumption, and these models can be classified into four main categories: the Patridge and Rowe model, the Kato-Wen model, the Kunii-Levenspiel model, and the modified Kunii-Levenspiel model. Caussat et al.[12] tested these four models with experimental data, concluding that the Kato-Wen model obtained the best agreement with the experimental data. They considered that the formation of the fine is mainly driven by the wall deposition of several polymeric Si species rather than the homogenous decomposition of silane, which disagreed with other studies[11;14]. However, this discrepancy could be generated by the conditions used in the experiment. Caussat et al.[26] used nitrogen as the carrying gas instead of hydrogen, which could lead to different results. Kojima et al.[27] developed a simplified two-phase model assuming that the bubble diameter is invariant along the reactor bed and is considered an adjusting parameter. Huang et al.[55] modified the two-phase model by considering the emulsion phase as a combination of several interconnected well-mixed CSTR reactors instead of one single ideally well-mixed reactor. This modification was validated with experimental data showing satisfactory results. Piña et al.[28] developed a multiphase gas-solid dynamic model for a spouted fluidized-bed reactor using the two-phase modeling approach proposed by Lai et al.[11]. They considered two adjacent regions, a spout zone (jet-emulsion zone) at the bottom of the reactor followed by a fluidized-bed region (bubble-emulsion zone). The main contribution of this work is utilizing the method of characteristics to discretize the population balance and predict the particle size distribution, while Lai et al.[11] employed the method of moments[18] to describe the dynamics of fines formation. Furthermore, Piña et al.[28] included a scavenging coefficient and an agglomeration constant as two adjustable parameters that must be determined by fitting experimental data for each case and correlated as a function of SiH_4 concentration. However, this model is limited to monodisperse distributions of seed particles that grow at the same rate.

These studies present detailed insights into the silane decomposition reaction mechanisms and diverse modeling approaches for FBR systems. However, few studies have focused explicitly on developing models that can be used to devise control strategies for silane pyrolysis in fluidized systems. White et al.[20] proposed a simplified model that can be easily tuned using experimental data, facilitating control purposes. They considered that both the heterogeneous decomposition reaction and the scavenging mechanism could contribute to the growth of silicon seed particles. Their work integrated feedback control theory into steady-state simulations to maintain a constant mass hold-up in the reactor and average product size. In addition, this study introduced a discrete representation of the population balance equation for the silicon particles, streamlining the modeling task. The changes in the particle size distribution are represented by discrete intervals based on average particle mass and number of particles. The discretization scheme and the control strategy proposed in this work have been utilized in further studies[3;35;56]. Nevertheless, the control strategies employed in these studies have focused solely on regulating mass hold-up and particle size distribution, overlooking the critical objective of minimizing powder loss to improve process yield.

2.5.3 Eulerian-Eulerian approach

Computational fluid dynamics (CFD) simulations provide a valuable approach to understanding the complex gas-solid interactions in the fluidized-bed reactor. Eulerian-Eulerian modeling is one of the most used approaches for fluidized systems due to its flexibility to handle large industrial-scale geometries[6]. This type of model generally considers both the gas and the solid phases as a fully interpreting continuum, solving the momentum, mass, and energy equations for both phases simultaneously[35]. The momentum conservation equations for solid and gas phases are given by:

$$\epsilon_g \frac{\partial}{\partial t}(\rho_g v_g) + \epsilon_g \nabla \cdot (\rho_g v_g v_g) = -\epsilon_g \nabla P + \epsilon_g \rho_g g - F \tag{2.12}$$

$$\epsilon_s \frac{\partial}{\partial t}(\rho_s v_s) + \epsilon_s \nabla \cdot (\rho_s v_s v_s) = -\epsilon_s \nabla P + \epsilon_s \rho_s g + F \tag{2.13}$$

Where ϵ_s and ϵ_g are the volume fraction of the gas and solid phase, while $v_s$and v_g denote the solid and gas phases velocities, respectively. The term F corresponds to the interface momentum transfer and the effects caused by the appearance or disappearance of chemical species in either the gas or solid phase[3]. Moreover, the mass balance is defined as:

$$\epsilon_g \frac{\partial}{\partial t}(c_i) + \epsilon_g \nabla \cdot (v_g c_i) = \nabla \cdot \left(D_{\text{eff},i} \frac{\partial c_i}{\partial x} \right) + R_i \tag{2.14}$$

The reaction rate of specie i is denoted by R_i, and c_i is the concentration of specie i. The term $D_{\text{eff},i}$ is the effective diffusivity of the specie i. Then, the energy balance equations for solid and gas phases are defined as follows:

$$\epsilon_s \frac{\partial}{\partial t}(\rho_s c_{ps} T_s) + \epsilon_s \nabla \cdot (\rho_s c_{ps} v_s T_s) = \nabla \cdot (k_s \nabla T_s) + Q_s - \gamma_{gs}(T_s - T_g) \tag{2.15}$$

$$\epsilon_g \frac{\partial}{\partial t}(\rho_g c_{pg} T_g) + \epsilon_g \nabla \cdot (\rho_g c_{pg} v_g T_g) = \nabla \cdot (k_g \nabla T_g) + Q_g + \gamma_{gs}(T_s - T_g) \tag{2.16}$$

where c_{pi} and k_{pi} are the heat capacity and thermal conductivity of specie i, respectively. The heat generated or consumed is represented by the term Q_i, while γ_{gs} corresponds to the heat transfer coefficient between the gas and solid phase. Benyahia et al.[57] provide a more detailed description of the governing equations and the transfer coefficients used in the calculations. Guenther et al.[29] simulated an FBR system for silane pyrolysis using the Multiphase Flow with Interphase eXchanges (MFIX) Software, which is an open-source CFD code developed by the National Energy Technology Laboratory for simulating fluidized systems using Eulerian-Eulerian approach[33]. Cadoret et al.[13] predicted the temporal and spatial evolution of local void fractions, particles, and gas velocities and the chemical vapor deposition of silicon from silane pyrolysis using MFIX. They performed 3-D simulations to describe the silane decomposition process in more detail, showing a significant improvement compared to the 2-D simulations. Then, Reuge et al.[30] performed multifluid Eulerian simulations utilizing MFIX and the same governing equations as Cadoret et al.[13]. However, their work improved in describing the heat transfer mechanism in the solid bed and determining which kinetic model is more appropriate for silane reaction. They concluded that there is a strong interaction between the chemical reaction and the bed hydrodynamics.

2.5.4 Discrete Element Method

The Eulerian-Eulerian approach has some limitations in modeling flows with a distribution of particle types and size because separate governing equations must be solved for each, increasing the computational cost extensively[6]. Moreover, Eulerian-Eulerian continuum models cannot capture the particle growth or size distribution unless integrated with population balance models[32;58]. Hence, the discrete element method (DEM) is an alternative to model fluidized bed reactors, which considers each particle as a tracking element and solves the fluid flow around the particle with the no-slip condition[6;59]. This type of model is also called the Eulerian-Lagrangian model. The advantage of the DEM approach is that it tracks the particles in the system, calculates the particle growth, and determines the size distribution of the seed particles. As a result, the particle growth by the CVD process and scavenging of fines can be more accurately captured by a DEM model rather than an Eulerian-Eulerian model. However, it is limited to a small number of particles and a small fluid domain due to the computational cost[6].

The DEM model can be coupled with mass transfer, heat transfer, and chemical reactions[60]. This combination can predict hydrodynamics, concentration and temperature profiles in both phases, particle growth, and size distribution. Hence, coupling the discrete element method with the Eulerian-Eulerian models represents a more comprehensive modeling strategy for FBR systems. Indeed, the combination of the DEM approach with Eulerian models is usually called the CFD-DEM coupling method or particle-in-cell (PIC) method, and it involves the benefits from both modeling perspectives. As the conventional DEM approach, the CFD-DEM model utilizes a fixed Eulerian grid and Lagrangian particles, but rather than solving the fluid flow around each particle, it considers the average of the fluid flow over a spatial region containing several particles[6].

A few studies considering this modeling approach to investigate silane decomposition in fluidized-bed systems have been reported in the literature. Parker[31] simulated the silane pyrolysis process in FBR using an experimental reactor set-up operated at the Jet Propulsion Laboratory (JPL) and using Barracuda, which is a software package utilized in the Computational Particle Fluid Dynamics (CPFD) numerical method for multiphase CFD calculations. A simplified kinetic model for silane pyrolysis is adopted in this study, consisting of the heterogeneous decomposition of silane onto Si particles and the homogeneous decomposition of silane into fines. The predicted temperature gradient along the solid bed by the proposed model was compared with the experimental measurements, showing a satisfactory agreement. In addition, the effect of the distributor was also analyzed, determining that the nozzle type inlet would create a more uniform gas distribution, which results in a better performance in the bubbling bed. The simulation results were validated with experimental data, showing consistency with the experimental results. Then, Chanlaor et al.[59] proposed a CFD-DEM coupling model to investigate silicon production via silane pyrolysis in a spouted bed reactor. Their study considered the same reaction pathways as Parker[31]'s work, but they differ in the expression for the scavenging rate. Chanlaor et al.[59] utilized a deterministic expression that relates the scavenging factor coefficient with the particle size and bed voidage[11]. In contrast, Parker[31] considered a constant scavenging factor coefficient value reported in previous experimental studies in the literature. The simulation results of solid movements by the CFD-DEM model were compared with experimental data and correlations, indicating a good agreement.

2.5.5 Multiscale Modeling Framework

Different temporal and spatial scales are involved in the dynamics of the silane-based FBR process. For instance, the silane decomposition is almost instantaneous and reaches completion over a few centimeters at the reactor's entrances[56]. The flow and mixing regimes stabilize into steady-state conditions within a few seconds of operation. In addition, the temperature can reach steady state conditions contingent upon the inlet conditions after a few minutes[3]. In contrast, the dynamics of particle size growth are slow, with changes in the particle size distribution taking over hours or days[24]. Hence, a multiscale modeling approach must be a suitable option to represent the system's behavior by linking the microscale and macroscale kinetics and transport effects. This approach improves the understanding of the process and enables the development of high-fidelity models by decomposing the system into distinct modules and developing information communication among them.

Balaji et al.[3] proposed a multiscale modeling framework for coupling the CFD solver COMSOL Multiphysics and MATLAB. Fig 2.5 shows the modeling strategy and the interconnection between the modules. The CFD module solves the hydrodynamics using COMSOL, obtaining temperature, porosity, and concentration profiles along the reactor. This information is used in the CVD module to estimate the overall process yield, which is the input to the population balance module. The PBM module describes the particle size distribution and computes the average particle size, which is imported into the CFD module to start a new calculation. The population balance model (PBM) module is based on the discretization scheme of the population balance equation proposed by White et al.[20].

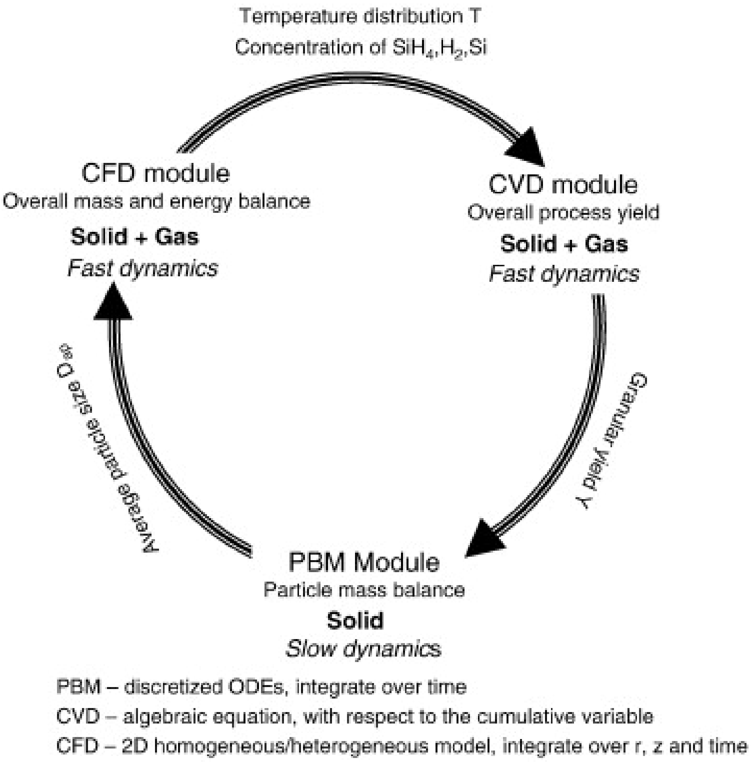

Figure 2.7: *Multiscale modeling framework*[3]

Du et al.[33] employed a similar modeling approach incorporating several modifications in the reaction module. Their work adapted the two-phase fluidized bed model developed by Lai et al.[11] to integrate information provided by the fluid dynamic module implemented in COMSOL. The model structure is illustrated in Fig 2.6. In this case, the CFD module computes the temperature distribution and the bed density as the solid volume fraction, and these profiles are the inputs for the reaction module to estimate the overall solid silicon production. The overall granular yield or deposition rate determines the particle growth rate, which is the critical parameter for the population balance to capture the dynamics of the particle-size distribution.

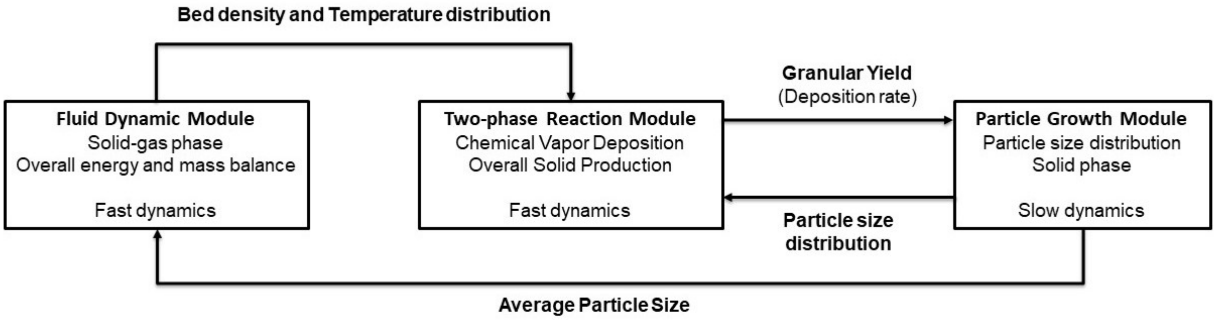

Figure 2.8: *Multiscale model structure*

The particle size distribution significantly impacts the fluidization behavior of the bed. Therefore, the fluid dynamic module periodically recomputes the hydrodynamics of the systems based on the new average particle size determined by the particle growth module. Liu and Xiao[32] proposed a coupled Eulerian-granular (CFD-PBM) model providing a comprehensive insight into the particle growth using 3-D simulation in the FBR process. Their work combines an Eulerian-Eulerian two-fluid model combined with a population balance model. The two-fluid model incorporates the kinetic theory of granular flow to solve the conservation equations for the hydrodynamics, while the population balance is solved using the quadrature methods of moments (QMOM) to describe the silicon particle growth. Gu et al.[61] developed a similar CFD-PBM modeling approach employing a different particle growth process considering the velocity difference between phases. In addition, their work explored extensively the effect of several operational conditions in promoting silicon deposition and reducing fine formation.

Chapter 3

Model Development

3.1 Silane pyrolysis

The silane decomposition temperature for silane is about 420°C[62]. Nevertheless, the kinetic energy of individual silicon atoms at this temperature is too low to form crystalline structure[63]. Therefore, the silane-based FBR systems usually operate at temperatures 650–800°C to ensure a crystalline structure and complete release of bonded hydrogen[36]. In general, silane decomposition in fluidized-bed reactors involves three main processes: heterogeneous decomposition, homogeneous decomposition, and scavenging. Fig 3.1 illustrates the processes involved in the silane-based fluidized bed reactor.

The heterogeneous decomposition is the preferred reaction, and it contributes directly to the particle growth via chemical vapor deposition when it reacts on the surface of the seed particles. The undesired reaction is the silane homogeneous decomposition because it produces an amorphous silicon powder, which can be lost through the gas phase[9]. The homogenous decomposition of silane occurs in the gas phase far away from the particle's surface. Hence, this reaction pathway does not contribute directly to the growth of seed particles. A fraction of the generated powder is scavenged by existing silicon particles and then recrystallized to contribute to the particle growth[20]. The scavenging mechanism removes a

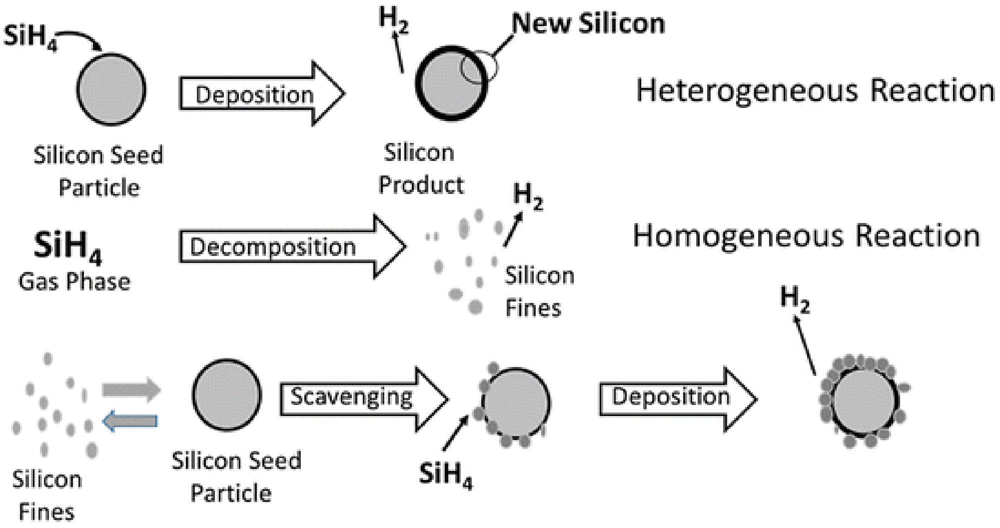

Figure 3.1: *Reaction mechanisms for silane pyrolysis*[4]

fraction of the silicon powder by accretion, and the fine particles chemically sinter onto the larger silicon particles aided by the heterogenous reaction[4]. The remaining powder is exhausted in the gas phase with unreacted silane and hydrogen, reducing the yield. Although the reaction mechanism is not entirely understood, Lai et al.[11] developed a comprehensive model to describe silane pyrolysis in fluidized bed reactors considering different reaction pathways involved in the particle growth. Fig 3.2 illustrates the reaction mechanisms in converting silane into solid silicon.

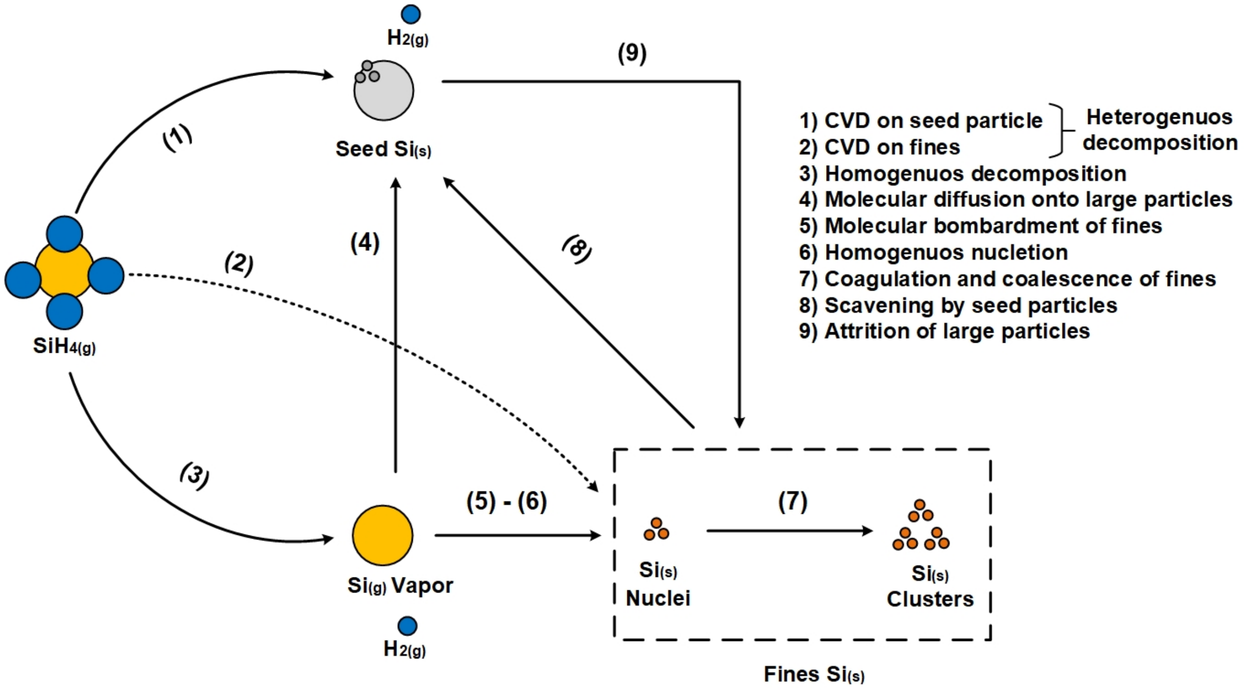

Figure 3.2: *Reaction pathways for conversion SiH_4 to solid Si*

The reaction scheme proposed by Lai et al.[11] shows several mechanisms involved in converting silane into silicon. Silane can react via heterogeneous decomposition onto the surface of the existing Si seed particles (pathway 1) or on the formed Si fines (pathway 2), leading to chemical vapor deposition. The CVD process controls the growth rate of large particles. The other primary reaction is the homogenous decomposition (pathway 3), which produces an intermediate gaseous species instigating the nucleation of a new silicon phase (fines). Silicon vapor is assumed to be the gaseous intermediate. The concentration of silicon vapor can be suppressed by diffusion and condensation on large particles (pathway 4) and molecular bombardment of fines (pathway 5)[11]. The nucleation of critical size Si nuclei (pathway 6) occurs whenever the supersaturation is exceeded[35]. The formed Si nuclei can coalesce (pathway 7) to create larger clusters of solid silicon (fines powder). The powder produced by the silicon vapor can be scavenged by larger Si particles and contributes to the particle growth. Changes in the particle size distribution can be caused by attrition (pathway 9) of large particles. However, this effect is negligible based on evidence from experiments[3;9].

These reaction pathways are used in practice to represent the reaction mechanism to produce silicon from silane. The expressions used to describe each pathway are discussed in the following sections.

3.2 Reaction Model

Silane undergoes thermal decomposition through two reaction mechanisms. The first involves homogenous decomposition into a gaseous intermediate, which is subsequently scavenged by seed silicon particles. The rate of homogeneous decomposition of silane is expressed by

$$r_{\mathrm{hom}} = 2 \times 10^{13} \exp\left(\frac{-26000}{T}\right) C_{\mathrm{SiH_4}} \tag{3.1}$$

The homogeneous decomposition generates an intermediate, promoting the nucleation of a new silicon phase (fines). Silicon vapor is assumed to be the gaseous intermediate. The silicon nucleation rate is described by the classical theory of homogeneous nucleation[64]

$$r_{\mathrm{HN}} = N_A \frac{\alpha_c}{\rho} \left(\frac{2\hat{\sigma} m}{\pi}\right)^{1/2} \exp\left(\frac{-4\pi \hat{r}^2 \hat{\sigma} N_A}{3RT}\right) c_{Si}^2 \tag{3.2}$$

where N_A is Avogadro's number and α_c is the condensation coefficient. The critical radius nuclei $\hat{r}$ is determined by

$$\hat{r} = \frac{2\sigma_{Si}}{\rho_p RT \ln S} \tag{3.3}$$

where $S = P_{Si}/P_{Si}^0$ is the supersaturation ratio and P_{Si}^0 is the silicon vapor pressure at equilibrium, determined by the following equation when the temperature is below 1685 K[65]:

$$\log(P_{Si}^0) = 7.5341 - 2.3399 \times 10^4/T \tag{3.4}$$

The specific surface energy ($\hat{\sigma}$) of condensed-phase silicon nuclei is approximated based on the surface tension at the melting temperature (σ_m)[66].

$$\hat{\sigma} = \sigma_m \left(\frac{7500 - T}{7500 - T_m} \right)^{1.2} \tag{3.5}$$

The concentration of silicon vapor is suppressed by diffusion and condensation on large particles and by molecular bombardment of powders. The rate of molecular diffusion of silicon vapor onto larger particles is expressed by[67]

$$r_{dl} = \frac{2D_g}{d_p}(C_{Si} - C_{Si}^0) \tag{3.6}$$

where D_g is the molecular gas diffusion coefficient calculated by

$$D_g = \frac{k_B T}{3\pi \mu d_{pf}} \tag{3.7}$$

with k_B is the Boltzmann constant, μ is the viscosity of the gas phase, and d_{pf} is the diameter of fine particles. The rate of molecular bombardment of silicon vapor on powder is also determined by

$$r_{df} = \left(\frac{RT}{2M_{si}} \right)^{1/2} (C_{Si} - C_{Si}^0) \tag{3.8}$$

A fraction of the fines generated due to silicon molecule nucleation are captured by larger particles, contributing to overall particle growth. The rate at which fines are scavenged can be estimated using the following expression,

$$R_{sc} = k_{sc} C_f \tag{3.9}$$

where C_f denotes the concentration of fines generated by nucleation and k_{sc} is the scavenging factor coefficient. The appropriate value for k_{sc} must be determined by comparing model predictions and experimental data[32].The proportionality constant $k_{\mathrm{sc}}\,[m^3/s]$ is within the range $0 \leq k_{\mathrm{sc}} \leq V_{\mathrm{g}}$[20]. However, Lai et al.[11] proposed an expression to relate the scavenging factor with the particle diameter (d_p) and the single large-particle collection coefficient (E).

$$k_{sc} = Eu_{mf}\frac{3(1-\epsilon_g)}{2d_p\epsilon_g} \tag{3.10}$$

where u_{mf} and ϵ_g are the minimum fluidization velocity and the bed void fraction, respectively. The single large-particle collection coefficient represents the overall capture efficiency from interception, impaction, and diffusion. In the FBR system, the predominant particle capture mechanism is diffusion[59]. Therefore, this coefficient can be related to the Peclet number (Pe) in terms of the mass transfer diffusion[11].

$$\begin{aligned} E &= 2Pe^{-\frac{2}{3}} \\ Pe &= \frac{d_p u_{mf}}{D_g} \end{aligned} \tag{3.11}$$

The second thermal decomposition reaction pathway involves the heterogeneous decomposition of silane occurring either on the surface of the pre-existing seed silicon particles or onto the fines generated, ultimately resulting in chemical vapor deposition[11].

$$r_{het} = \frac{5.14\times10^9}{6(1-\epsilon_b)/d_p}\exp\left(\frac{-19530}{T}\right)C_{\mathrm{SiH_4}} \tag{3.12}$$

Where ϵ_b is the void fraction of the bed and d_p is the particle size. The previous reaction rate equation is expressed in terms of the volume of the solid bed. However, it can be converted in terms of the surface area of particles considering the experimental conditions of the study[11;68]:

$$r_{het} = 2.79\times10^8\exp\left(\frac{-19530}{T}\right)C_{\mathrm{SiH_4}} \tag{3.13}$$

Therefore, the overall decomposition rate of silane is expressed by:

$$R_{total} = r_{het}(A_{tl}+A_{tf}) + r_{hom}V_g \tag{3.14}$$

where V_g denotes the gas phase volume, calculated as the difference between the total reactor volume (V) and the volume occupied by the solid phase (V_s). The volume of the solid phase is determined by the density of solid silicon, with an assumption of negligible porosity in the solid particles, where $V_s = M_{solid}/\rho$ and M_{solid} and ρ represent the amount of solid silicon and its density, respectively. Subsequently, A_{tl} denotes the available surface area of the larger particles (seed particles), while A_{tf} represents the available surface area of fine particles (powder). The surface area of seed particles (A_{tl}) is assessed using the population balance equation, as elaborated in the subsequent section. Conversely, for the surface area of fines (A_{tf}), an approximation is made by considering the average diameter (d_{pf}) of fine particles found in the literature[33]. The increase in silicon particle size within the reactor is facilitated through direct chemical vapor deposition onto the surface of seed particles and the incorporation of fines generated during the reaction. Consequently, the overall deposition rate (Y) on seed particles is a combination of the heterogeneous decomposition rate (r_{het}), the molecular diffusion rate of silicon vapor (r_{dl}), and the scavenging rate (R_{sc}).

$$Y = A_{tl}(r_{het} + r_{dl}) + R_{sc} \tag{3.15}$$

A portion of the fines produced remains unscavenged by the larger particles. This residual powder is transported out of the reactor alongside hydrogen and silane in the gas phase, increasing the yield loss. The proportion of unrecovered fines, often referred to as powder loss, can be assessed by considering it as a function of both the total deposition rate and the reaction rate of silane.

$$F_f = 1 - \frac{Y}{R_{total}} \tag{3.16}$$

3.3 Flow regime and mass balances

3.3.1 Well-mixed flow regime

The fluid dynamics and gas-solid interactions within the fluidized reactor present inherent complexities. Nonetheless, under certain operational conditions, the system's behavior can be reasonably approximated as that of an ideally well-mixed reactor (CSTR). This approximation becomes feasible in fluidized beds only when bubble formation is effectively suppressed while ensuring good solid-gas mixing[11;20]. Assuming well-mixed conditions for both the solid and gas phases within the reactor, the mass balances for the gas phase are expressed as follows

$$\begin{aligned}
\frac{dM_{\mathrm{SiH_4}}}{dt} &= F^{in}C^{in}_{\mathrm{SiH_4}} - F^{out}C^{out}_{\mathrm{SiH_4}} - (r_{hom}V_g + r_{het}(A_{tl} + A_{tf})) \\
\frac{dM_{\mathrm{H_2}}}{dt} &= F^{in}C^{in}_{\mathrm{H_2}} - F^{out}C^{out}_{\mathrm{H_2}} + 2(r_{hom}V_g + r_{het}(A_{tl} + A_{tf})) \\
\frac{dM_{\mathrm{Si}}}{dt} &= (r_{hom} - r_{hn})V_g - r_{dl}(A_{tl} + A_{tf}) \\
\frac{dM_f}{dt} &= r_{hn}V_g - R_{sc} - F^{out}C^{out}_f + r_{het}A_{tf}
\end{aligned} \tag{3.17}$$

This particle growth system involves several distinct time scales. The silane decomposition reaction is almost instantaneous and reaches completion over a few centimeters at the reactor's entrance[26]. The flow and mixing regimes stabilize into steady-state conditions within a few seconds of operation. Additionally, contingent upon the inlet conditions, the temperature can attain a steady state after a few minutes[3]. In contrast, particle size growth proceeds at a markedly slower pace, with changes in the particle size distribution taking place over days[24]—consequently, Eqs. 3.17 can be solved under pseudo-steady state conditions.

3.3.2 Plug flow regime

The assumption of an ideal mixed-flow reactor can only be applied to describe system dynamics under particular conditions. However, experiments indicate that the process yield may exhibit variability based on the prevailing process conditions, from concentration gradients within the fluid phase, or inconsistent operational parameters[3;24]. Notably, the existing equations within the CSTR framework fail to account for the gas phase concentration gradients across the reactor. To offer a more encompassing representation of the system's dynamics, the gas phase is proposed to be modeled as a plug-flow reactor under pseudo-steady state conditions. This adjustment aims to capture the nuanced dynamics of the gas phase within the reactor, which are essential for a comprehensive understanding of the system

$$
\begin{aligned}
\frac{dM_{\mathrm{SiH_4}}}{dx} &= -r_{hom}V_g - r_{het}(A_{tl} + A_{tf}) \\
\frac{dM_{\mathrm{H_2}}}{dx} &= -2\big(r_{hom}V_g + r_{het}(A_{tl} + A_{tf})\big) \\
\frac{dM_{\mathrm{Si}}}{dx} &= (r_{hom} - r_{hn})V_g - r_{dl}(A_{tl} + A_{tf}) \\
\frac{dM_f}{dx} &= r_{hn}V_g - R_{sc} + (r_{dl} + r_{het})A_{tf}
\end{aligned}
\tag{3.18}
$$

In this case, both the silane decomposition rate and total deposition rate depend on the reactor height (h). Integrating these parameters into the discrete population balance scheme requires the calculation of their respective average values, as expressed by:

$$
\begin{aligned}
R_{total} &= \frac{1}{h}\int \big(r_{het}(x)(A_{tl} + A_{tf}) + r_{hom}(x)V_g\big)\, dx \\
Y &= \frac{1}{h}\int \Big(A_{tl}\big(r_{het}(x) + r_{dl}(x)\big) + R_{sc}(x)\Big)\, dx
\end{aligned}
\tag{3.19}
$$

3.4 Population balance equation

The dynamics implied in the production of polysilicon in FBR systems are characterized by the production scale, growth rate, and the co-presence of a dispersed phase within a continuous phase. These processes involve complex physico-chemical phenomena, including particle nucleation, coagulation, growth, and breakage, as the two phases coexist, influencing the spatial distribution of properties such as size, shape, molecular weight, and porosity[17]. In particulate processes, the distribution of properties takes place across both external (space and time) and internal (particle size) coordinates[18]. Hulburt and Katz[69] used a statistical mechanics theory to develop a continuous phase space description of the particulate system behavior. As a result, they proposed the population balance equation to explain the evolution of particles in phase space. The population balance equation (PBE) describes the "conservation of probability" (i.e., the number density of particles) in the phase space[20]. The evolution of these properties along the external coordinates is described by the population balance equation:

$$\frac{\partial n}{\partial t} + \nabla \cdot (\vec{v}n) - B + D = 0 \tag{3.20}$$

where n represents the particle distribution function, and the term $\nabla \cdot (\vec{v}n)$ corresponds to the change of particles along the external and internal coordinate axes. The birth or death of particles due to agglomeration or attrition is represented by B and D terms, respectively. However, in combination with the mass balance equation of the continuous phase, it results in a set of partial integro-differential equations that are challenging to solve. Several numerical methods have been proposed for solving this set of equations, including moment transformation[19], discretization approaches[20], orthogonal collocation[21], and method of weighted residuals[18]. Discretization methods have been proposed for predicting particulate systems such as crystallization and emulsion polymerization[17;22;23].

Typically, the solution methods initially simplify the population balance equation to obtain a tractable approximation of the general equation that can be solved for a given initial and boundary conditions. In particular, White et al.[20] developed a novel system of ordinary differential and algebraic equations to approximate the population balance equation. The proposed approach uses the particle mass and number balances over discrete intervals. The discretization approach is illustrated in Fig. 3.3. Hence, the discrete population balance tracks the particle movement through discrete size intervals to simulate changes in the size distribution[9]. This discrete representation of the population balance equation ensures the preservation of conservation laws along discretization levels, reducing the computational costs without additional discretization[20]. Notably, this approach converges to the classical population balance equation when the number of discrete intervals approaches infinity[9;20].

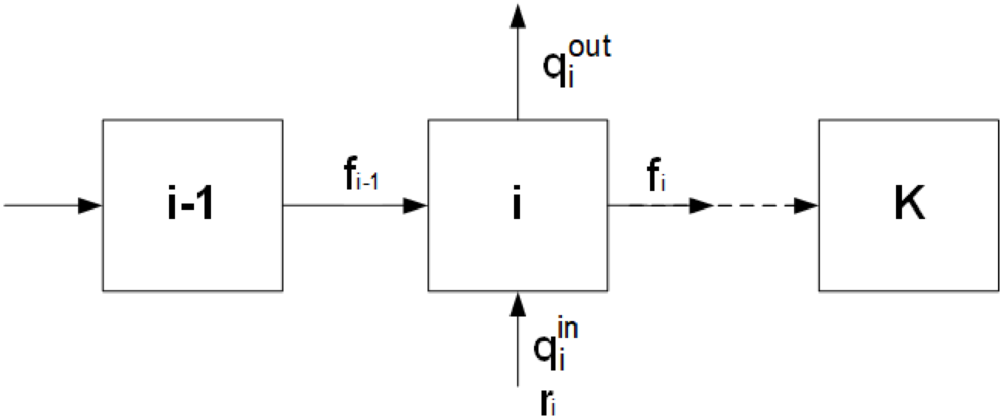

Figure 3.3: *Discrete size interval network.*

The analysis assumes that particles are distributed across K discrete intervals (classes). Each class is usually known as a class, characterized by an average number of moles (or mass) per particle. Consequently, each class contains a specific number of particles denoted as N_i, with an average mass m_i. The correlation between the overall mass of the particles and the amount of particles within each interval is expressed as

$$M_i = m_i N_i \quad \forall i = 1, 2, \ldots, K \tag{3.21}$$

Thereby, the total available surface area of the particles in a class is defined as

$$A_i = a_i N_i \tag{3.22}$$

where a_i represents the surface area of a particle within the size class i. Experimental measurements have reported that the shape of silicon particles closely approximates a sphere. Hence, the surface area of a particle with diameter l is calculated by the following expression

$$a_i = 4\pi \left(\frac{l}{2}\right)^2 \tag{3.23}$$

Particle growth is initiated through deposition onto the particles and a scavenging process, prompting their transition from one size interval to the subsequent size category. Consequently, the mass balance for each size interval is articulated as follows

$$\frac{dM_i}{dt} = f_{i-1} + f_i + r_i + q_i \tag{3.24}$$

The conservation equation for the quantity of particles within each class is expressed as

$$\frac{dN_i}{dt} = \frac{q_i}{m_i} - \frac{f_i}{m_i} + \frac{f_{i-1}}{m_i} \tag{3.25}$$

where $q_i = q_i^{\text{in}} - q_i^{\text{out}}$ represents the total external flow of particles. It is defined as the difference between the rate of addition of seed particles q_i^{in} within the class i and the particle withdrawal flow q_i^{out} from each class.

The rate of mass transfer from the gas phase to the solid phase within each class is expressed as

$$r_i = Y \frac{A_i}{\sum_i A_i} \quad \forall i = 1, 2, \ldots, K \tag{3.26}$$

The key parameter connecting the rate of silane decomposition to particle growth in the population balance is the total deposition rate Y. The deposition rate in each class is proportional to the available surface area of the silicon particles in the class. Molar flows of particles occur between consecutive particle size classes. The molar flow entering the size interval i is denoted as f_{i-1}, whereas f_i represents the molar flow existing in the class. Notably, this study does not consider the effects of agglomeration and attrition. White et al.[20] developed an expression linking molar flows between neighboring classes,

$$f_i = r_i \frac{m_{i+1}}{m_{i+1} - m_i} \tag{3.27}$$

Nevertheless, the final class K requires additional considerations. According to the mass balance illustrated in Eq. 3.27, this concluding class should not involve particle flow to the subsequent class. Consequently, the mass balance and number balance for class K are defined as

$$\frac{dM_i}{dt} = f_{i-1} + r_i + q_i, \quad \frac{dN_i}{dt} = \frac{q_i}{m_i} + \frac{f_{i-1}}{m_i + 1} \tag{3.28}$$

The final class K has no mass transfer from the fluid phase to the solid particles. The total mass is the cumulative sum of all masses across all classes

$$M_{\text{total}} = \sum_{i=1}^{K} M_i \tag{3.29}$$

The comprehensive mass balance equation for the solid phase is expressed as follows

$$\frac{dM_{\text{total}}}{dt} = Y + S - P \tag{3.30}$$

where S is the seed addition rate, Y is the total deposition rate, and P is the product withdrawal rate. Sustaining a consistent level in the solid bed is crucial for ensuring the stable operation of the reactor. A constant bed hold-up implies that the bed has a constant pressure drop, which indicates stable fluidization. This goal can be achieved by controlling the total mass hold-up of silicon particles within the reactor. The regulation of the total mass hold-up is facilitated by manipulating the flow of product withdrawal. Therefore, a passivity-based inventory control strategy for the silicon mass hold-up[24] can be defined as

$$\frac{dM_{\text{total}}}{dt} = K_m(M_{\text{total}} - M^*) \tag{3.31}$$

where K_m is a proportional gain constant and M^* is the desired mass hold-up. Consequently, the expression for product withdrawal can be formulated as

$$P = S + Y + K_m(M_{\text{total}} - M^*) \tag{3.32}$$

The proposed control strategy effectively regulates the mass hold-up in the system, taking into account the product withdrawal rate. The average particle size is determined by employing the weighted average approach, derived from the particle size distribution,

$$d_p = \frac{1}{\sum_i w_i/d_{pi}} \tag{3.33}$$

where w_i represents the fraction (weight) of i-th interval in the distribution, and d_{pi} denotes the particle diameter.

Chapter 4

Model Predictive Control

Model predictive control (MPC) is an advanced control technique implemented extensively in the industry[70;71] and studied in academia[72–74]. It is based on a real-time optimization problem of a mathematical model of the system. Moreover, MPC is one of the few control strategies able to manage systems with constraints determining an optimal control for a specific performance index[75]. In particular, this control technique is a suitable option for the control design of highly complex multivariable processes[71;76;77]. MPC relies on a system model to predict future system dynamics by incorporating it into the optimization process, determining the optimal sequence of control actions. Hence, MPC determines the control law through a model-based optimization problem, avoiding the tedious formulation of explicit implied in conventional control techniques[71]. The anticipating behavior and capacity to handle constraints make MPC a valuable and useful control strategy for real systems.

4.1 Theory

Model predictive control is an advanced control strategy capable of predicting future process states to estimate optimal control actions within the constraints of the process[76–78]. It is based on a repeated real-time optimization of a mathematical system model[74]. Fig 4.1 shows a simplified block diagram of a control loop using an MPC controller. Initially, the controller receives or estimates the current state of the actual system (y). Then, based on the system model, the MPC predicts the future system behavior considering the optimal sequence of manipulated variables (u) obtained by solving a constrained optimization problem to achieve a desired state or reference (r).

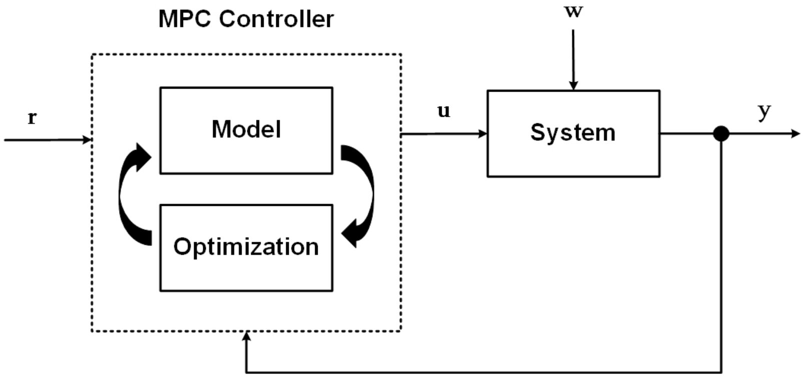

Figure 4.1: *Block diagram of MPC-based control loop*

The objective of MPC is to minimize a predefined cost function while satisfying constraints such as system dynamics[71]. This is one of the few control strategies that directly considers constraints. Fig 4.2 presents a schematic view of the MPC operation. The cost function is formulated so the system output y tracks a given reference. At each time step, the controller computes the best control actions u that minimize the cost function over a specific time horizon[5]. Only the first computed control input action is implemented in the actual system. Then, a new measure from the state is sampled, and the calculations of predictions and optimizations are repeated from a new current state. Hence, these prediction and optimization tasks are repeated at each time instance, shifting the prediction horizon forward. This is the reason why MPC is usually also called receding horizon control.

The combination of prediction and optimization is the key difference from conventional control methods, which used precomputed control laws[79]. Furthermore, MPC presents other advantages compared to traditional control approaches. For instance, it can manage multiple inputs and outputs, an essential characteristic of complex systems. Moreover, it can handle system constraints, ensuring the system states and control actions remain within acceptable

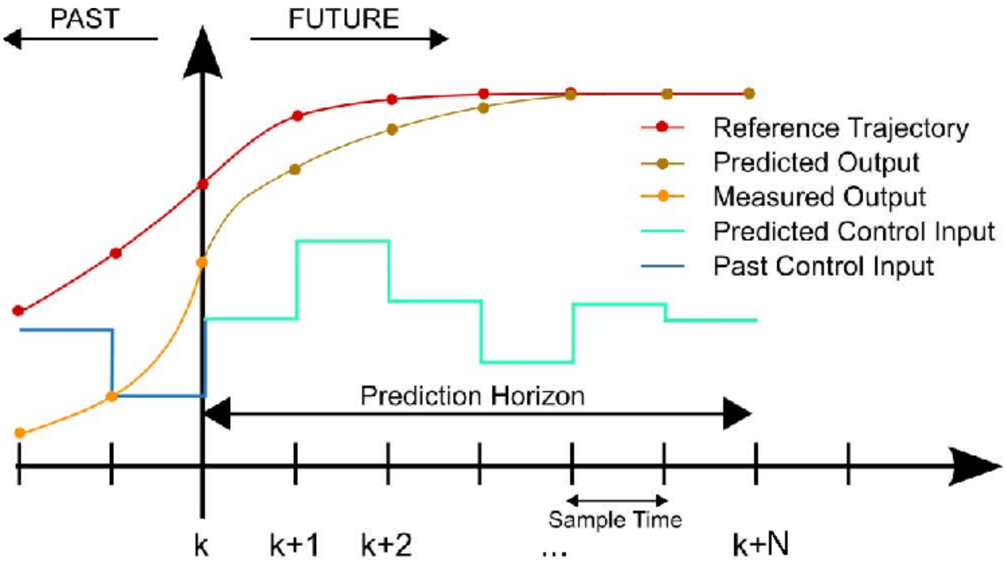

Figure 4.2: *Receding horizon concept of MPC*[5]

bounds. Consequently, MPC has been widely used in several industrial applications.

4.2 Mathematical Formulation

MPC consists of three integral components: an objective function, a process model, and a dynamic optimizer. Leveraging the process model, MPC predicts the system's state response by considering the inherent physical phenomena. Subsequently, real-time optimization comes into play, determining the optimal control action by resolving the following dynamic optimization problem:

$$\min_{u} \; J\big(x(t), u(t)\big) = \int_{t}^{t+T_p} F\big(x(\tau), u(\tau)\big)\, d\tau \tag{4.1}$$

subject to the nonlinear process model

$$\dot{x}(t) = f\big(x(t), u(t)\big), \quad x(0) = x_0 \tag{4.2}$$

and input and state constraints

$$\begin{aligned} u(\tau) &\in \mathcal{U} \quad \forall \tau \in [t, t+T_c] \\ x(\tau) &\in \mathcal{X} \quad \forall \tau \in [t, t+T_p] \\ C(x, u, t) &= 0 \\ D(x, u, t) &\leq 0 \end{aligned} \tag{4.3}$$

where

$$\begin{aligned} \mathcal{U} &:= \{u \in \mathbb{R}^m \,|\, u_{\min} \leq u \leq u_{\max}\} \\ \mathcal{X} &:= \{x \in \mathbb{R}^n \,|\, x_{\min} \leq x \leq x_{\max}\} \end{aligned} \tag{4.4}$$

where $x(t) \in \mathbb{R}^n$ and $u(t) \in \mathbb{R}^m$ represent the state and input vectors, respectively. The vectors $u^{\max}$ and $u^{\min}$ denote the upper and lower bounds for the manipulated inputs, while $x^{\max}$ and $x^{\min}$ specify the upper and lower bounds for the state vector. T_p and T_c represent the prediction and control horizons, respectively, where $T_c \leq T_p$. The functions C and D encompass nonlinear vector functions that correspond to the equality and inequality constraints inherent in the system. The cost function J under consideration is quadratic,

$$F\big(x(\tau), u(\tau)\big) = (x - x_s)^T Q (x - x_s) + (u - u_s)^T R (u - u_s) \tag{4.5}$$

where x_s and u_s represent the desired reference vector values (targets) for the system state and manipulated inputs, respectively. These reference values may be constant or time-varying. The positive definite weight matrices $Q \in \mathbb{R}^{n \times n}$ and $R \in \mathbb{R}^{m \times m}$ are adjusted to impose penalties on the errors in state regulation and manipulated variables within the objective function[80]. The system model utilized to predict the response is initialized based on the actual system state, which can be either directly measured or estimated. Solving the optimization problem yields the optimal sequence of control actions $u^*(\cdot, x(t)) : [t, t+T_p] \rightarrow \mathcal{U}$ over the prediction horizon $[t, t+T_p]$. Then, the computed vector of manipulated variables during the prediction horizon is applied, with only the first control input of the sequence being implemented at time t. Subsequently, the optimization process recommences for the next sampling period.

4.3 Robust Model Predictive Control

MPC predicts the system's state response by considering the inherent physical phenomena. Since these models are used to predict the system's behavior, an error is usually associated with non-linearities or estimations. Therefore, the controller must deal with uncertainties representing model inaccuracy, disturbances, or estimation errors[81]. The MPC scheme that explicitly considers the uncertainties to calculate the optimization problem is called Robust MPC (RMPC). The main attribute of RMPC is stabilizing the system to the desired target regardless of uncertainties. Hence, this scheme guarantees a satisfactory performance even in the presence of model mismatch or additive disturbances.

Different strategies to design robust MPC controllers have been developed. The feedback min-max approach is a well-known strategy incorporating robustness to the MPC controller to manage uncertain systems by considering the worst-case scenario[82;83]. Hence, in the context of the min-max approach, the optimization problem is solved by minimizing the maximum possible value of the cost function (worst-case scenario), considering all possible realizations of uncertainties within a specified set. It prepares for the most adverse effects of uncertainties or disturbances on system performance. Therefore, the system remains stable and performs optimally even under adverse conditions. This approach is beneficial in situations where the system is subject to uncertainties and is required to guarantee a certain level of performance, even in the worst-case scenario. Subsequently, determining the optimal control action is based on solving a dynamic optimization problem defined as follows[84]:

$$\min_{u} \; J\big(x(t), u(t)\big) = \min_{u} \int_{t}^{t+T_p} \max_{w \in \mathcal{W}} F\big(x(\tau), u(\tau)\big)\, d\tau \tag{4.6}$$

subject to the nonlinear process model

$$\dot{x}(t) = f\big(x(t), u(t), w(t)\big), \quad x(0) = x_0 \tag{4.7}$$

and input and state constraints

$$\begin{aligned} u(\tau) &\in \mathcal{U} \quad \forall \tau \in [t, t + T_c] \\ x(\tau) &\in \mathcal{X} \quad \forall \tau \in [t, t + T_p] \\ C(x, u, t, w) &= 0 \\ D(x, u, t, w) &\leq 0 \end{aligned} \tag{4.8}$$

where

$$\begin{aligned} \mathcal{U} &:= \{u \in \mathbb{R}^m \,|\, u_{\min} \leq u \leq u_{\max}\} \\ \mathcal{X} &:= \{x \in \mathbb{R}^n \,|\, x_{\min} \leq x \leq x_{\max}\} \\ \mathcal{W} &:= \{w \in \mathbb{R}^p \,|\, w_{\min} \leq w \leq w_{\max}\} \end{aligned} \tag{4.9}$$

where $x(t) \in \mathbb{R}^n$ represent the system state, $u(t) \in \mathbb{R}^m$ is the input control action, and $w(t) \in \mathbb{R}^p$ corresponds to the uncertainty or disturbance. The vectors $u^{\max}$ and $u^{\min}$ denote the upper and lower bounds for the manipulated inputs, $x^{\max}$ and $x^{\min}$ specify the upper and lower bounds for the state vector, $w^{\max}$ and $w^{\min}$ specify the upper and lower bounds for the uncertainty. The robust MPC aims to minimize the worst-case cost, considering all possible disturbance sequences within a specified set over the prediction horizon T_p. The functions C and D encompass nonlinear vector functions that correspond to the equality and inequality constraints inherent in the system.

The min-max problem seeks to find a sequence of control inputs that minimizes the maximum possible cost, thus ensuring robustness against the worst-case disturbances. Solving the RMPC using the min-max approach can be computationally expensive due to the need to consider all possible disturbance sequences. However, it provides a conservative control approach to ensure a suitable performance even for the worst-case scenario during operation.

Chapter 5

Results and Discussion

5.1 Well-mixed regime and Plug-flow regime

This section discusses the results obtained using the ideal well-mixed conditions and the plug-flow regime. Table 5.1 outlines the simulation parameters employed in this study. In our investigation, we utilized 20 size intervals. The average particle size within each interval is documented in a prior study[9]. The associated initial bed distribution and seed size distribution are depicted in Fig. 5.1.

Table 5.1: *Well-mixed regime vs Plug-flow regime: Initial Conditions.*

Parameter	**Value**	**Symbol**
Reactor height	7 m	h
Reactor diameter	0.5 m	D
Inlet gas velocity	0.55 m/s	v_{in}
Inlet Concentration - Silane	6.5 mol/m^3	$C_{\text{SiH}_4}^{\text{in}}$
Inlet Concentration - Hydrogen	1.6 mol/m^3	$C_{\text{H}_2}^{\text{in}}$
Inlet Concentration - Silicon Powder	0.001 mol/m^3	$C_{\text{Si}}^{\text{in}}$
Scavenging factor	0.03 m^3/s	k_{sc}
Fine diameter	$0.3 \times 10^{-6} m$	d_{f}
Seed addition rate	0.001 mol/s	S
Initial Solid bed	350 kg	M
Mass hold-up	450 kg	M^*
Reactor Temperature	850 K	T

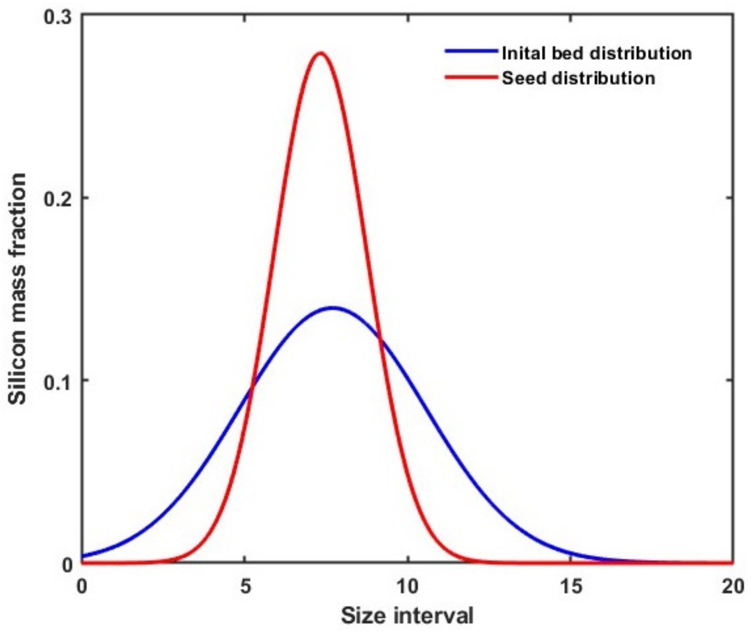

Figure 5.1: *Particle size distributions used for the simulations.*

5.1.1 Open-loop simulations

Fig. 5.2 illustrates the open-loop particle growth dynamics, showing the evolution of the key process properties over time. The simulation results indicate that the particle growth dynamics reach steady state conditions after 125 hours. Fig. 5.2a displays the average particle sizes predicted by both modeling approaches. While minimal differences exist in the steady-state values obtained from both models, a notable disparity emerges in the transient region. The mismatch is associated with the different deposition rates calculated in each modeling approach. The well-mixed flow regime approach reaches steady-state conditions faster due to a higher initial deposition rate. In contrast, the plug flow regime approach yields a lower deposition rate due to incorporating concentration gradients in the calculations.

The evolution of the particle size distribution due to the particle growth reduces the available surface area for chemical vapor deposition onto the seed particles. A significant reduction in the available surface area of seed particles is observed in Fig. 5.2b. This reduction in surface area diminishes the effectiveness of chemical vapor deposition generated from the heterogeneous decomposition of silane and the molecular diffusion of silicon vapor

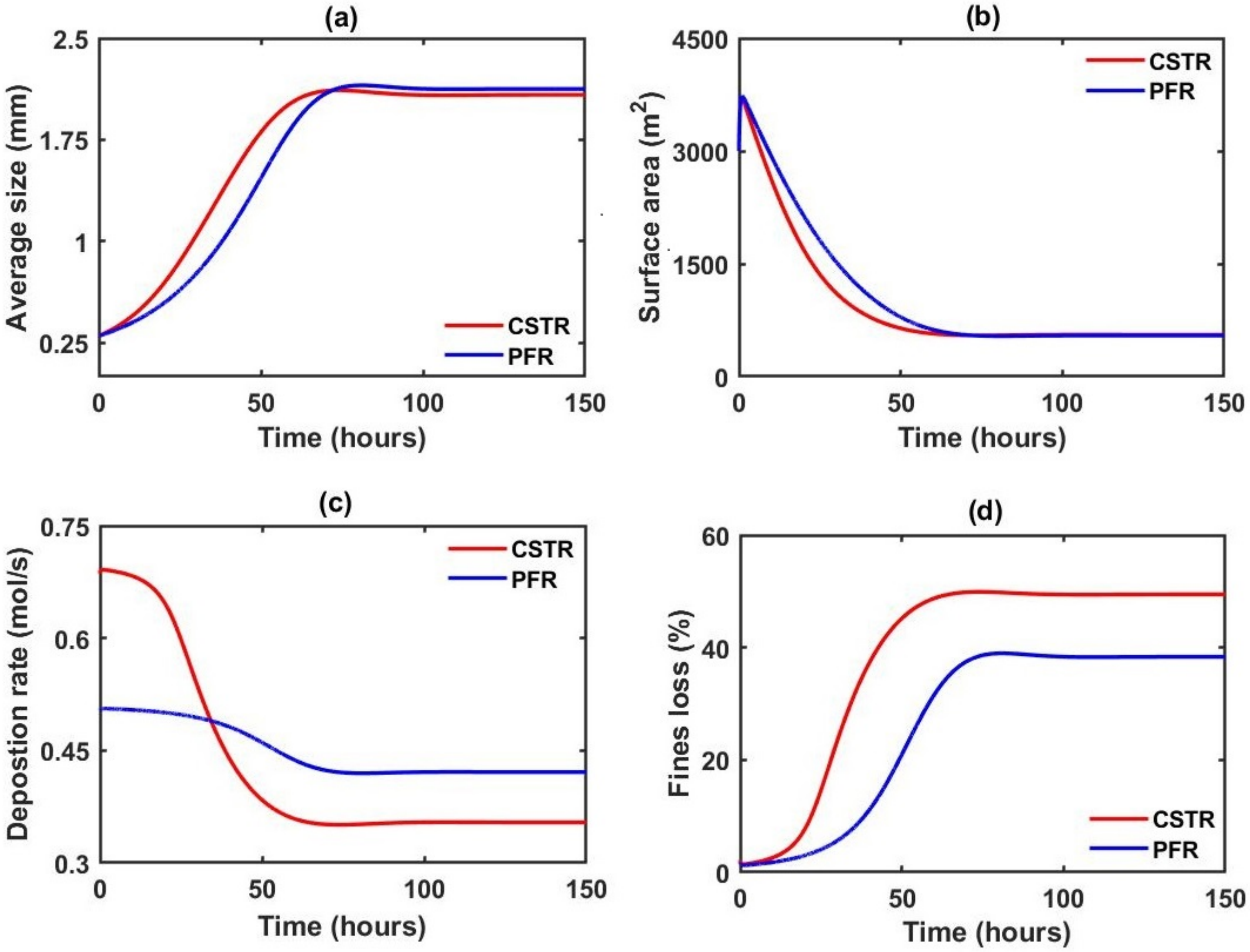

Figure 5.2: *Well-mixed regime vs. Plug-flow regime: (a) average particle size, (b) available surface area, (c) total deposition rate, and (d) powder loss.*

to facilitate particle growth. Thereby, there is a substantial reduction in the overall deposition rate predicted by both models (Fig. 5.2c). However, there is a significant difference in the deposition rate predicted by each model. The well-mixed regime approach initially estimates a higher deposition rate than the plug flow regime approach. This initial response is due to the assumption of a uniform composition through the reactor, where the well-mixed condition induces a complete silane reaction in the gas-solid interphase. However, after a few hours, the well-mixed approach predicted a prominent drop in the deposition rate.

In contrast, the deposition rate predicted by the plug-flow regime approach shows a slight reduction over time. In both cases, this reduction is caused by reducing the available area of the seed particles due to particle growth. However, the generation of fines is a significant factor related to the deposition rate. Due to the ideal-mixed condition, the well-mixed regime approach estimates a higher fines production. Consequently, it also predicts a higher powder loss, as shown in Fig 5.2d. As a result, less silane is decomposed into silicon via heterogeneous decomposition, which diminishes the deposition rate. Moreover, this behavior is more visible when both models reach steady-state conditions.

Figure 5.2d showcases the predicted powder loss for each modeling approach. Both models estimate a powder loss exceeding 40% of the generated powder under steady-state conditions. However, the well-mixed flow approach predicts a higher power loss. Minimizing powder loss is imperative to enhance the process yield. Several factors contribute to increased powder loss, including elevated temperatures, which promote fine formation due to the higher activation energy of the homogeneous decomposition reaction compared to the heterogeneous mechanism. The scavenging factor also significantly influences powder loss and deposition rate. For these simulations, a constant scavenging factor is considered based on experimental measurements[20;56]. However, this factor can change during the operation due to the variation of the particle size distribution and minimum fluidization conditions. Additionally, higher inlet gas velocities can carry more fine particles in the gas phase at the top of the FBR system. Consequently, operating at high temperatures or increased inlet gas velocities leads to a diminished process yield.

Generally, at low temperatures and low gas flow rates (near the minimum fluidization velocity), the predictions of these two models align closely. However, achieving the ideal well-mixed condition, especially at minimum fluidization conditions, is challenging in practice. Furthermore, the well-mixed flow regime modeling approach oversimplifies the system by neglecting concentration and temperature gradients in its calculations. In contrast, the plug flow regime approach offers a more accurate system representation, making it suitable for control and decision-making.

5.1.2 Closed-loop Simulations

The prediction and control horizons are set to $N_p = N_c = 10$ sampling, with a sampling time of $\Delta = 5$ hours for each MPC iteration. Therefore, the prediction horizon for solving the optimal control problem at each sampling instance is determined as $T_p = T_c = 50$ hours. It is assumed that all states are accessible at the designated sampling times. The control objective is stabilizing the system at the steady-state condition detailed in Table 5.2.

Table 5.2: *Case Study 1 and Case Study 2: Steady State Values.*

Parameter	Value	Symbol
Mass hold-up	450 kg	x_1^{SS}
Average Particle size	2.10 mm	x_2^{SS}
Seed addition rate	0.001 mol/s	u_1^{SS}
Inlet gas velocity	0.55 m/s	u_2^{SS}

The interior-point optimization algorithm (IPOPT) is employed to address the nonlinear constrained dynamic optimization problem at each sampling time[85;86]. Given the nonconvex nature of the optimization problem, the assurance of a global minimum value is not guaranteed. A substantial number of iterations and function evaluations are considered to mitigate this, ensuring that the optimization process does not conclude prematurely before converging to the optimal solution. Weight matrices are utilized to balance the importance of each state and input variable in the cost function. However, in this context, mass holdup and particle size distribution are deemed equally significant, as are the manipulated inputs. Consequently, identity matrices are chosen for weight matrices Q and R. The controlled variables encompass the product's mass holdup and particle size distribution, crucial for ensuring the system's proper operation. Maintaining a constant mass holdup is essential for stable fluidization within the reactor. However, the non-self-regulating nature of the mass holdup dynamic necessitates constraints to avoid convergence to different steady states or instability when determining associated flow rates. Eq. 3.32 is integrated into the MPC controller as a nonlinear constraint to regulate the product withdrawal rate.

The second controlled variable is the particle size distribution of the product. The physico-chemical and mechanical properties of particulate system products hinge strongly on the characteristics of the corresponding particle size distribution[17]. Manipulating the particle size distribution is thus fundamental for controlling product quality. The product size distribution depends on the seed added to the reactor and the ratio between the seed mass and the total mass. Hence, the seed addition rate can be used as a manipulated variable. The seed addition rate influences the product size distribution, while the inlet gas velocity regulates the deposition rate by controlling the amount of silane in the reactor.

Additionally, these manipulations can be considered to minimize power loss in the FBR system. Consequently, the seed addition rate and the inlet gas flow rate are manipulated inputs for the MPC controller, constrained within ±50% of their steady-state values outlined in Table 5.2. For the closed-loop simulations, two case studies are considered for the MPC implementation. The first scenario assumes the implementation of nominal MPC without a mismatch between the process model and the actual system. The second scenario illustrates the implementation of robust MPC when there is a mismatch between the process model and the actual system.

5.1.3 Case Study 1

It considers no mismatch between the process model used in the nominal MPC for the calculations and the actual system where the control actions determined in the optimization problem are implemented. The plug flow regime approach is considered in both the process model and the actual system. Hence, no uncertainties or disturbances are considered in this case. Fig. 5.3 illustrates the closed-loop simulation employing the plug flow regime model approach. State variables and inputs are presented in normalized deviation form. Figs. 5.3a and 5.3b depict the seed addition rate and the inlet gas velocity gradually converging to their steady-state values. After 50 hours, the control actions reach a steady-state condition, remaining constant.

Fig. 5.3c presents the dynamic response of the mass holdup, revealing a faster dynamic

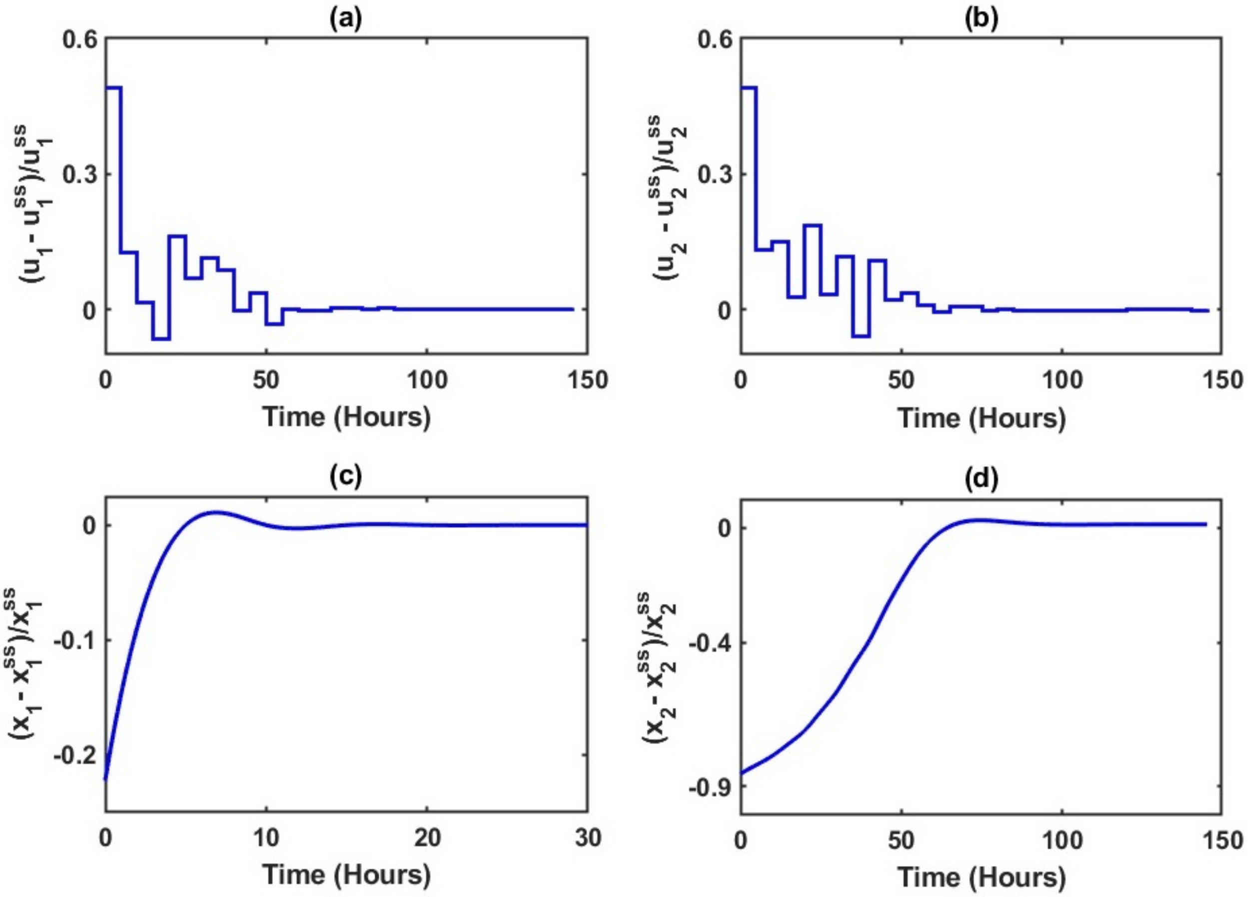

Figure 5.3: *Case Study 1 - Closed-loop system dynamics: (a) seed addition rate, (b) inlet gas velocity, (c) mass holdup, (d) average particle size.*

response compared to the average particle size illustrated in Fig. 5.3d. A slight overshoot is observed before the system attains its steady-state value. This overshooting behavior results from the control strategy outlined in Eq. 3.32, integrated with MPC. Turning attention to Fig. 5.3d, the transient response in the particle size distribution is evident, requiring a more extended period to achieve a steady-state condition. The sluggish evolution of the average particle size can be attributed to the gradual dynamics inherent in the particle growth process. In summary, both state variables exhibit convergence with smooth trajectories, indicating the successful stabilization of the system at their respective steady-state values.

5.1.4 Case Study 2

The second case study considers a mismatch between the process model and the actual system. This case presents a more realistic situation for the robust MPC implementation, where the process model provides a simplified representation of the actual system. In this case, the well-mixed flow regime approach is employed as the process model for the controller calculations, and the plug flow regime approach is considered as the actual system. Hence, in this case, the controller must consider uncertainties or disturbances associated with the process model. Based on the open-loop simulation illustrated in Fig 5.4, these uncertainties could be related to the discrepancy in the deposition rate predicted by each model. In this case, the RMPC considers an uncertainty within the range ±0.2 for the deposition rate calculated by the well-mixed flow regime approach. Fig. 5.4 shows the closed-loop response of the system considering the mismatch in the RMPC calculations.

The seed addition rate and inlet gas velocity are shown in Fig 5.4a and Fig 5.4b, respectively. In this case, the controller reaches the steady-state value for the seed addition and inlet gas velocity following smoother and more gradual trajectories, even considering the mismatch between both models. In addition, the controller can reach the steady-state value for manipulated input slightly faster than in the previous case study. The control actions reach a steady-state condition before 50 hours. This result can be caused by considering a simpler model in the RMPC calculations, which also shows faster dynamics and reaches the steady-state conditions in less time. These process model features could reduce the optimization complexity, allowing the controller to converge faster to the optimal point.

The transient response of the mass holdup is presented in Fig. 5.4, which describes a similar dynamic response compared to the previous case study. Focusing on Fig. 5.4d, the particle size distribution reaches the steady-state condition slightly faster than the results obtained in Fig. 5.4d. Generally, both state variables demonstrate an equivalent behavior to the results obtained in case study 1. Therefore, these results indicate that the RMPC controller can stabilize the system to their steady-state values, even considering the mismatch

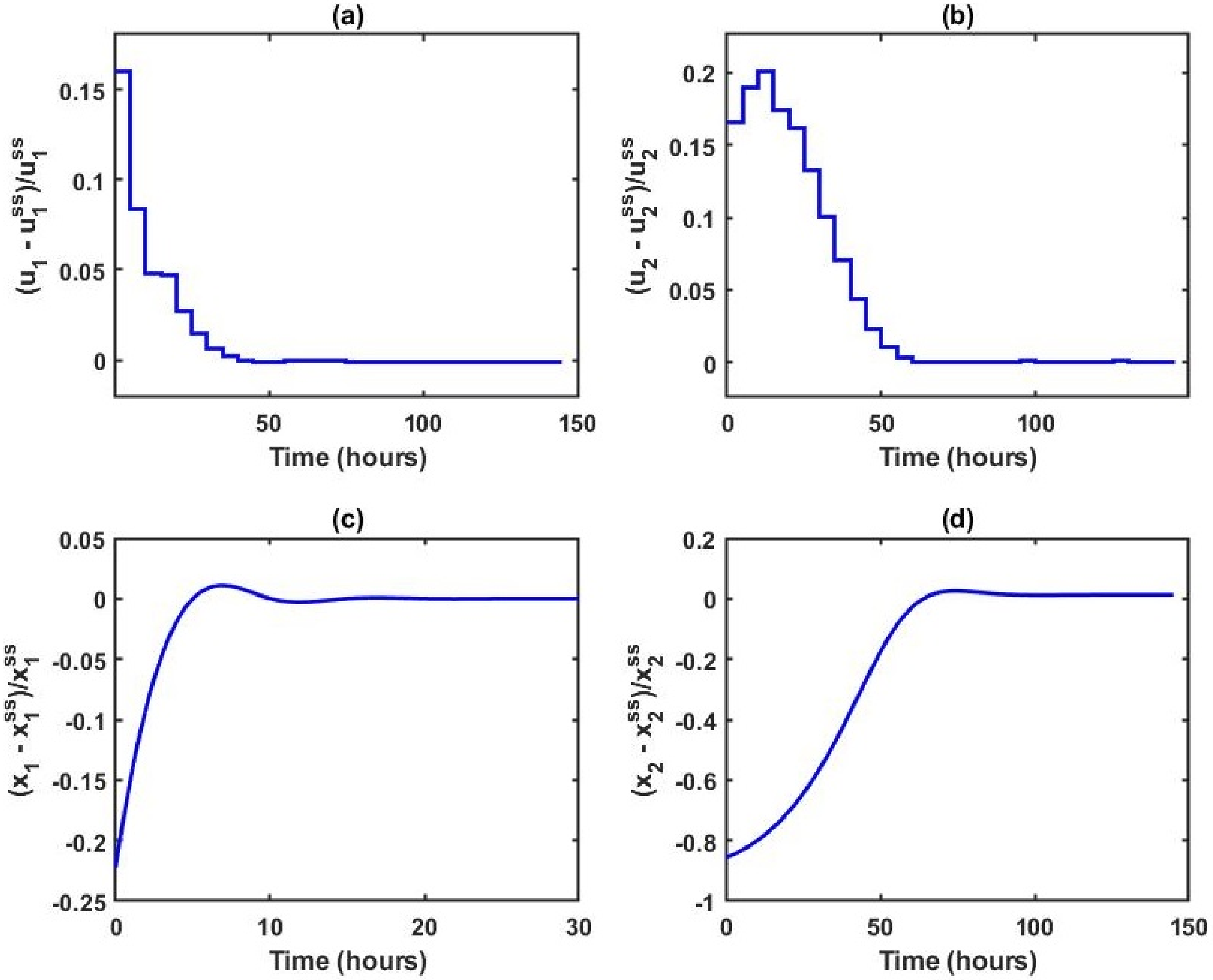

Figure 5.4: *Case Study 2 - Closed-loop system dynamics: (a) seed addition rate, (b) inlet gas velocity, (c) mass holdup, (d) average particle size.*

between the process model and the actual system. However, the discrepancy between these models can be more considerable under different parameters and operational conditions.

5.2 Modified plug-flow regime

The modeling approaches discussed in the previous section are simplified representations of the FBR system. In particular, they considered a constant scavenging factor (k_{sc}) and a homogenous distribution of the reactor temperature. These are coarse assumptions that can oversimplify the description of the actual system. Therefore, a modified plug-flow regime is considered to obtain a more comprehensive model. Hence, an energy balance for the gas phase reactor was incorporated in the model, and the scavenging factor is periodically estimated using Eq 3.10 under system conditions.

The energy balance for the gas phase is given by:

$$\frac{dT}{dV} = \frac{r_A \Delta H_{Rx} - UA(T - T_r)}{(\sum_i F_i C_{P_i})} \tag{5.1}$$

where r_A is the reaction rate expression. In particular, this term is represented by the overall reaction rate (Eq 3.14). Then, ΔH_{Rx} is the reaction enthalpy, U is the overall heat transfer coefficient, and A is the heat exchange area per unit volume of the reactor ($A = D/4$). Finally, T_r and T correspond to the reactor wall and gas phase temperatures, respectively. In particular, it assumed that the temperature of the solid phase is the same as the gas phase. This is a reasonable assumption supported by prior research[56;87].

The energy balance is incorporated into the model to capture the temperature gradient in the FBR system. However, this modification also adds a new variable, which is the reactor wall temperature. This variable can be used as a manipulated input to control the system during the desired operation. Therefore, some simulations for studying the dynamics of the modified plug-flow model at different reactor wall temperatures are considered. The parameters used in the open-loop simulations are summarized in Table 5.3.

5.2.1 Open-loop simulations

The dynamic behavior of the FBR system evaluated at different reactor wall temperatures is presented in Fig 5.5. In general, the reactor temperature has a significant effect on the particle growth dynamics. Fig5.5a illustrates the average particle size predicted by the model, showing different results, especially in the transient region. At a low temperature of 800K, slower particle growth is observed, indicating that the deposition rate is favored at high temperatures. However, there is no significant difference between the dynamics obtained

Table 5.3: *Modified plug-flow reactor: Initial Conditions.*

Parameter	**Value**	**Symbol**
Reactor height	6 m	h
Reactor diameter	0.3 m	D
Inlet gas velocity	0.55 m/s	v_{in}
Inlet Concentration - Silane	6.5 mol/m^3	$C_{\text{SiH}_4}^{\text{in}}$
Inlet Concentration - Hydrogen	26 mol/m^3	$C_{\text{H}_2}^{\text{in}}$
Inlet Concentration - Silicon Powder	0.001 mol/m^3	$C_{\text{Si}}^{\text{in}}$
Reaction Enthalpy	2000 J/mol	ΔH
Fine diameter	$0.3 \times 10^{-6} m$	d_{f}
Seed addition rate	0.001 mol/s	S
Initial Solid bed	350 kg	M
Mass hold-up	450 kg	M^*
Reaction Enthalpy	2000 J/mol	ΔH
Overall heat transfer coefficient	150 W/m^2K	U
Inlet gas Temperature	500 K	T

at 900 K and 950 K. The fastest particle growth is obtained at 850 K, obtaining a larger average particle size in the transient region. However, there is no significant difference in steady state conditions. This result is observed due the average particle size is controlled by the mass holdup and seed addition rate used in the FBR system. However, the transient region is governed by the deposition rate obtained from the silane pyrolysis. The evolution of the available surface area is displayed in Fig 5.5b. The increment in the average particle size cause a significant reduction in the available surface area. This reduction leads to a decrement in the contribution of the CVD process and molecular diffusion of Si vapor in the deposition rate. In addition, in contrast to the results obtained in the previous section (Fig 5.2), the modified plug-flow regime model shows slower particle growth dynamics, reaching steady state conditions after 150 hours. Furthermore, the average particle size at steady state predicted by the modified plug-flow model (1.9 mm) is slightly smaller compared to the simplified version (2.10 mm).

Fig 5.5c presents the deposition rate obtained at different reactor temperatures. In general, a depletion of the deposition rate during the operation is observed as being caused by

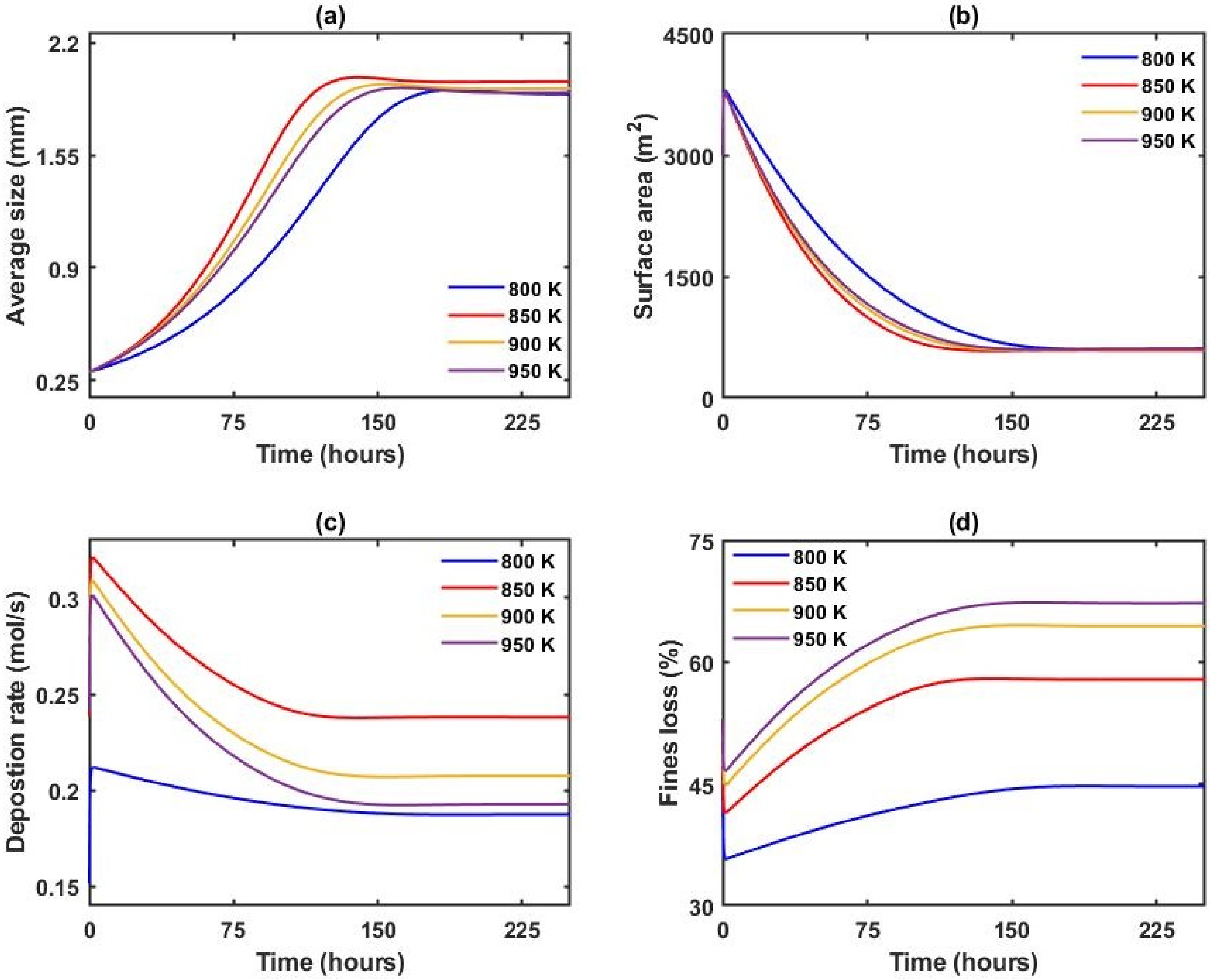

Figure 5.5: *Open-loop system dynamics: (a) average particle size, (b) available surface area, (c) total deposition rate, (d) free fines.*

the reduction of the available surface area. The lowest deposition rate value is obtained at 800 K, which produces the slower dynamic shown in Fig 5.5a. Conversely, the highest deposition rate is achieved at 850 K, generating the fast dynamics in the particle growth. However, at higher temperatures than 850 K, it is observed that the deposition rate decreases, leading to slower particle growth. This reduction is caused by the homogeneous decomposition pathway favored at high temperatures, which produces more powder and interferes with the CVD mechanism. This effect is more evident when analyzing the powder loss in Fig 5.5d. It presents the fraction of powder loss over time, indicating an increment in the fine loss as the reactor temperature increases. Therefore, the desired performance can be obtained by controlling the reactor temperature to reduce the power loss.

Fig5.6 depicts the dynamic of the modified plug-flow model in the spatial coordinates. Fig 5.6a shows the temperature profile of the gas phase obtained at different reactor wall temperatures. In every case, The temperature of the gas phase reaches the reactor wall temperature after a distance of 2m in the reactor height. However, there is a peak in the temperature profile, which is more noticeable at higher temperatures. It is produced by the exothermic effect of the silane pyrolysis, which is more significant because the effect of the homogeneous decomposition is more favored at these conditions. In contrast, this effect is insignificant at lower temperatures (800 K), where the silane pyrolysis mainly occurs via heterogeneous reaction.

The silane concentration in the gas phase is presented in Fig 5.6b, showing a higher and faster conversion at high temperatures. At reactor temperatures above 850 K, the silane conversion mainly occurs at the entrance of the reactor. Moreover, silane conversion is almost complete before reaching a reactor distance of 2 m at reactor wall temperatures higher than 850 K. This difference is caused by the influence of the homogeneous decomposition at high temperatures. Conversely, a significant amount of unreacted silane is observed at 800 K, indicating that silane pyrolysis is promoted at high temperatures. This effect is more evident in the concentration profiles of the intermediate Si vapor species in Fig 5.6c. In particular, it is assumed that Si vapor is only produced by homogeneous decomposition of silane. Hence, the concentration of this chemical species is expected to increase as the reactor wall temperature increases because the homogeneous decomposition reaction is favored at high temperatures. However, there is a low concentration of Si vapor during FBR operation. The concentration of this chemical specie is mainly suppressed by two pathways. First, it is consumed to form silicon nuclei, which leads to powder formation. Second, the Si vapor can diffuse and condense onto large Si particles and fines. In addition, the concentration of silicon fines is illustrated in Fig 5.6d, indicating that the highest concentration of fines is obtained at the highest temperature (950 K). This result confirms that homogeneous decomposition is

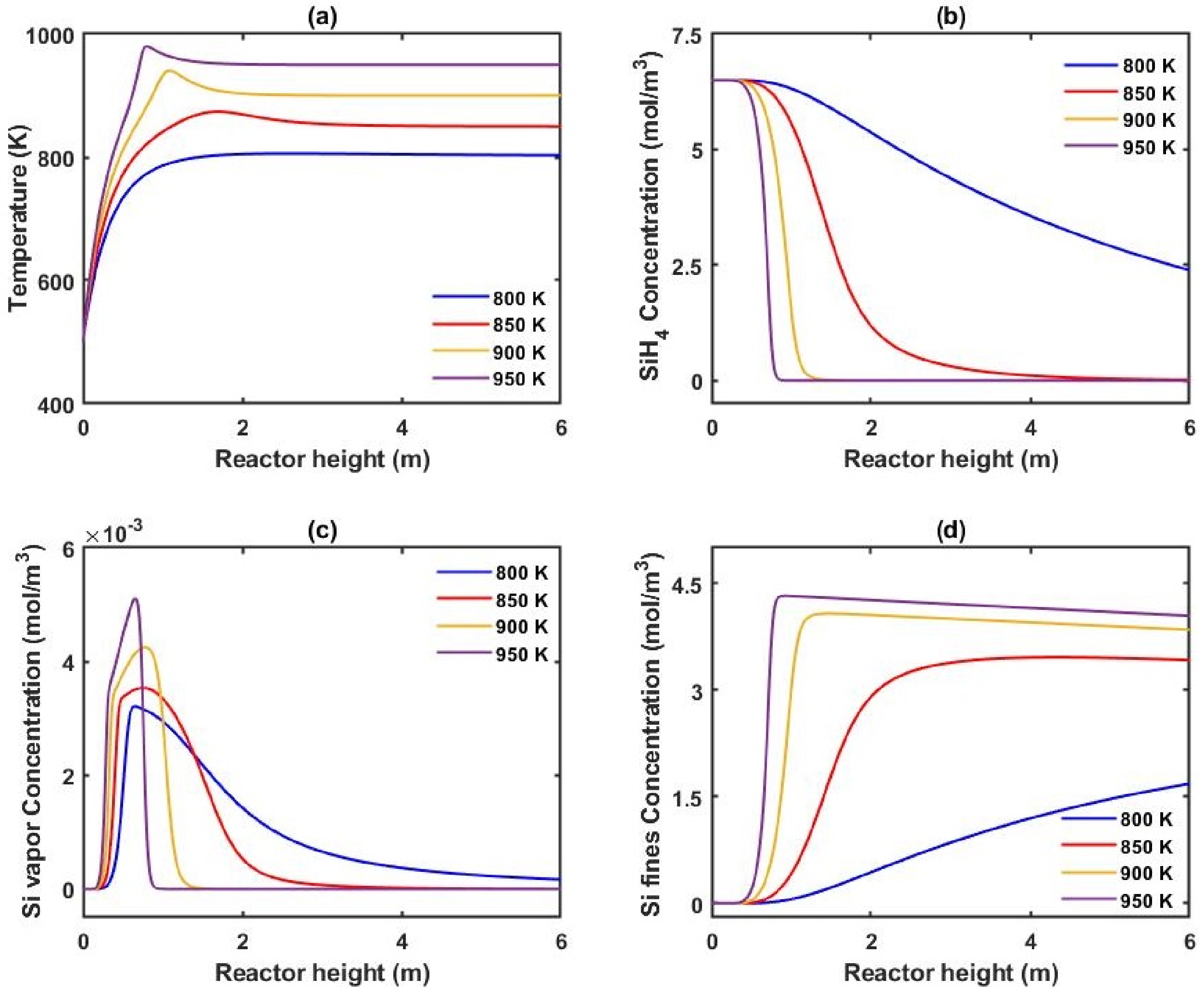

Figure 5.6: *Spatial coordinates dynamics: (a) Gas temperature, (b) SiH_4 concentration, (c) Si vapor concentration, (d) Si powder concentration.*

more important at higher temperatures. Furthermore, there is a slight reduction in the fine concentration profiles for 900 K and 950 K. This reduction is associated with the fraction of the scavenged powder by the larger particles. The scavenging effect is more pronounced at higher fine concentrations because it is proportional to the amount of powder in the reactor.

The evolution of the mass and number of particles in each discrete interval is presented in Fig 5.7. The change in the mass distribution and the number of particles at 850 K is considered in this case. In Fig 5.7a, it is observed that initially, the particle mass distribution is mainly accumulated in the middle region of the classes following a normal distribution.

Every discrete class has a mass increment at the initial hours of operation. Then, after a few hours, the silicon particles gradually move from smaller particle size classes to larger intervals, increasing the mass holdup inside the system. After 100 hours, the total mass holdup in the FBR system mostly accumulates in the discrete class 20, which is the largest size class. This accumulation in the last class is caused by not flowing to a subsequent particle size interval, resulting in no further particle growth beyond this point.

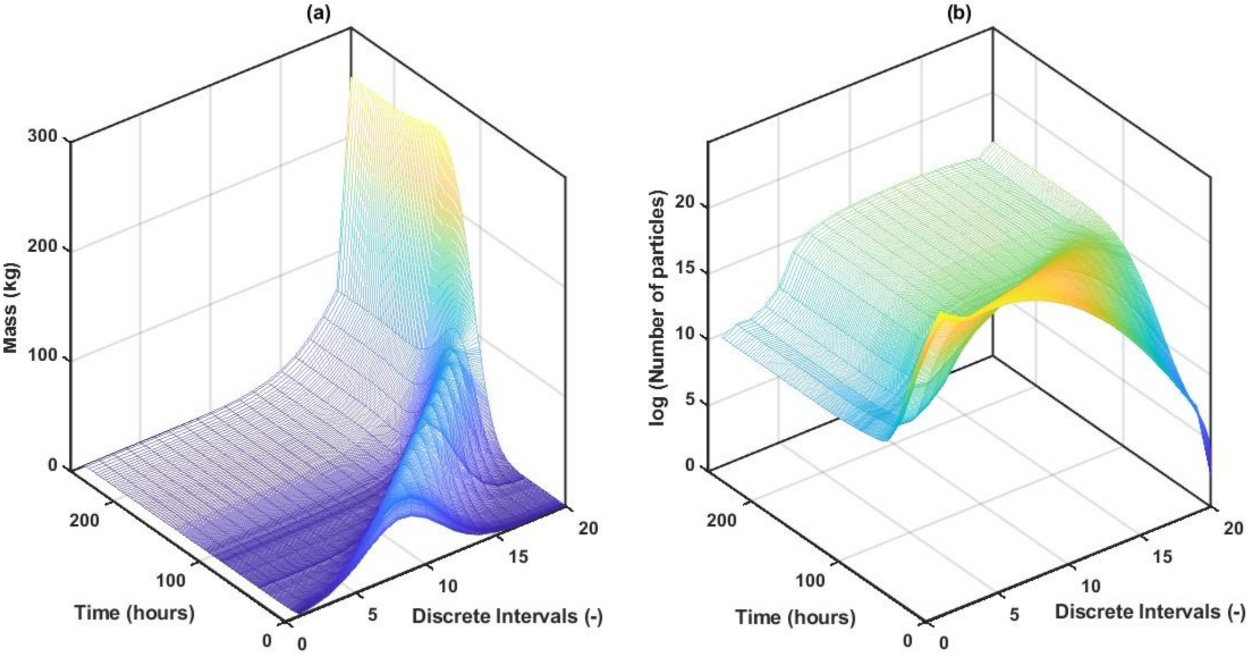

Figure 5.7: *Dynamic behavior in each discrete interval at 850 K: (a) Mass distribution, (b) Number of particles*

The number of particles per class is shown in Fig 5.7b. Despite the mass distribution being mainly condensed in the middle classes, the smaller classes from 1 to 5 contain a larger fraction of the total particles than the middle classes. This extensive presence of small particles provides a large available surface area for the chemical vapor deposition of solid silicon. After a few hours, the number of small particles decreases rapidly, moving to the next size classes due to the particle growth. Despite the significant difference in the mass and the number of particles in each class, it is important to mention that in the population balance model used in this study, the effect of attrition or breakage is not considered. As a result, particles have no transition from large particle size classes to smaller particle size classes. Consequently, the movement of particles is strictly forward from the small particle size class to the subsequent size class. This result is observed in both the mass and the number of particle distributions. However, the seed addition rate feeds new particles to the system continuously, maintaining a constant mass holdup and number of particles.

5.2.2 Closed-loop Simulations

The prediction and control horizons are set to $N_p = N_c = 10$ sampling, with a sampling time of $\Delta = 5$ hours for each MPC iteration. Therefore, the prediction horizon for solving the optimal control problem at each sampling instance is determined as $T_p = T_c = 50$ hours. It is assumed that all states can be measured at every sampling time. Table 5.5 contains the desired steady-state conditions for stabilizing the system.

Table 5.4: *Case Study 3: Steady State Values.*

Parameter	Value	Symbol
Mass hold-up	450 kg	x_1^{SS}
Average Particle size	1.90 mm	x_2^{SS}
Seed addition rate	0.001 mol/s	u_1^{SS}
Inlet gas velocity	0.55 m/s	u_2^{SS}
Reactor wall temperature	850 K	u_3^{SS}

Similar to the previous case studies discussed in section 5.1.3 and section 5.1.4, the IPOPT algorithm is used to address the nonlinear constrained dynamic optimization problem at each sampling time[86]. Furthermore, the mass holdup and particle size distribution are considered equally significant, as are the manipulated inputs. Therefore, identity matrices are selected for weight matrices Q and R. The mass holdup and the average particle size are the controlled variables that are essential to ensure a stable fluidization condition in the system operation. The main difference from the previous case study is incorporating the reactor wall temperature as another manipulated input in the MPC controller, increasing the degrees of freedom for MPC calculations. As a result, the seed addition rate, inlet gas velocity, and reactor wall temperature are the manipulation input variables. These manipulated inputs are constrained within ±50% of their steady state values for solving the optimization problem. Based on the non-self-regulating dynamics of the solid phase, Eq. 3.32 is considered a nonlinear constraint to regulate the product removal rate.

5.2.3 Case Study 3

In this case, no model mismatch or external disturbances are considered in the nominal MPC calculations. The modified plug-flow model is used as the process model and the actual system. Fig 5.8 shows the closed-loop simulations using the modified plug-flow model.

The inputs and state variables are presented in the normalized deviation form. Similar to the previous cases of study, Fig 5.8a and Fig 5.8b depict the seed addition rate and inlet gas velocity gradually converging to their steady-state values. Both input variables converge to their steady state values relatively fast. In fact, after the first iteration, the MPC controller can almost achieve the steady-state value for both manipulated variables. In particular, the observed deviation is bounded within the ±10% range from the steady-state value in both cases. There are some oscillations around the steady-state value. However, there is not a significant deviation from the steady-state value. These oscillations can be associated with the numerical errors and tolerance used in the optimizer. After 100 hours, it is observed that both manipulated variables reach a relative constant value. The deviation observed in both variables after this point is less than 0.2% with respect to their steady-state value.

Fig 5.8c shows the reactor wall temperature employed by the MPC controller during the closed-loop simulation. Like the other manipulated variables, the reactor wall temperature gradually converges to a steady-state value. After 100 hours, the reactor wall temperature converges to the desired steady-state condition and remains constant. Incorporating the reactor wall temperature as a manipulated variable increases the degree of freedom for the MPC controller in the optimization problem. With a greater degree of freedom, the controller has more options to manipulate the process variables, improving the responsiveness and

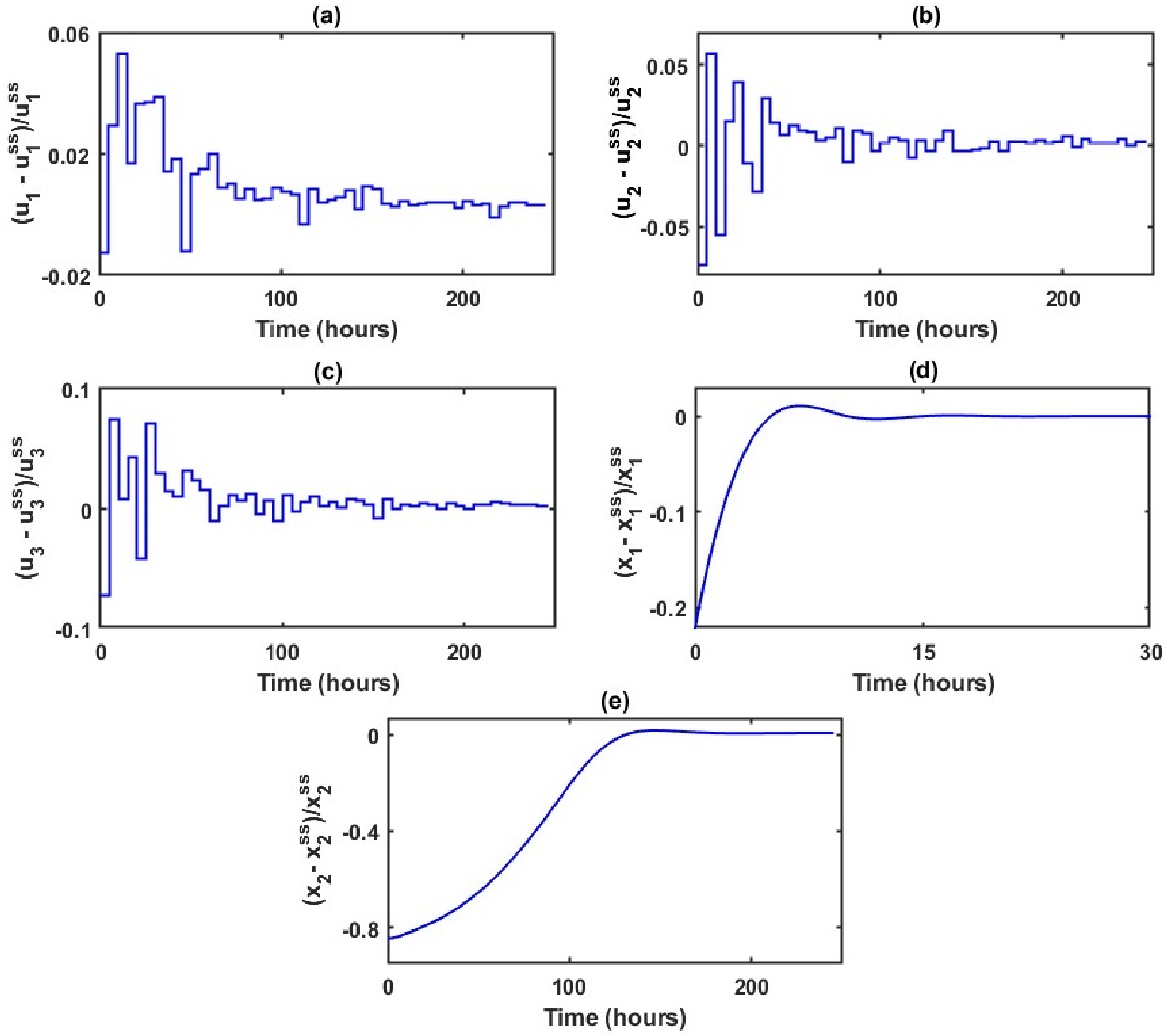

Figure 5.8: *Case Study 3 - Closed-loop system dynamics: (a) seed addition rate, (b) inlet gas velocity, (c) Reactor wall temperature, (d) mass holdup, (e) average particle size.*

effectiveness of the control system. Fig 5.8d and Fig 5.8e depict the dynamics corresponding to the mass holdup and the average particle size, respectively. The dynamic response of the mass holdup is displayed in Fig. 5.8d, indicating a faster dynamic response compared to the average particle size illustrated in Fig. 5.8e. This overshooting response is also observed in the previous cases of study, and it is produced by a feedback control strategy (Eq. 3.32), which is integrated with the MPC controller as a nonlinear constraint. However, the behavior of the transient response can be regulated by tuning the proportional gain (K) used in Eq.

3.32. This case study illustrates the feasibility of implementing a nonlinear MPC controller in the FBR system, considering the reactor wall temperature as a manipulated input.

The temperature of the gas phase in the FBR system has a major effect on the overall yield of the process. In fact, it regulates the deposition rate and the powder loss during the operation. Therefore, controlling the reactor temperature is an essential step in improving the polysilicon production in the FBR system. Moreover, this control system configuration can be enhanced by employing advanced control strategies focused on optimizing the economic benefit by maximizing the production yield from the process. Hence, economic model predictive control (EMPC) represents a promising alternative for future studies to optimize the economic performance of the FBR system by minimizing the powder loss rather than merely regulating it around a desired setpoint. EMPC directly targets the optimization of an economic objective, attempting to integrate economic process optimization and process control[88]. Hence, the formulation and selection of the cost function in EMPC is a critical step; it must represent the economic performance of the process. The objective function can be to minimize costs or maximize profit during operation. In the case of polysilicon production in FBR systems, the cost function for EMCP can be defined in terms of the powder loss to maximize the overall yield.

5.3 Modified plug-flow regime and Two-phase model

To validate the proposed model, the results obtained with the modified plug-flow model were compared with the multiscale two-phase model presented by Dutta[56], which is a reliable and comprehensive representation of the FBR system for silane pyrolysis. They develop a multiscale framework that uses the two-phase model proposed by Lai et al.[11] to calculate the deposition rate, the population balance model developed by White et al.[20] to track the particle size distribution, and COMSOL Multiphysics (Eulerian-Eulerain model) to describe the hydrodynamics of the system. In particular, the two-phase model uses the solid volume fraction and temperature distribution from COMSOL to estimate the deposition rate. Due to the extensive computational cost implied in executing the entire framework, they performed several COMSOL simulations at different average particle sizes to establish correlations between the temperature and void fraction as a function of reactor height at various particle sizes. These correlations are polynomial functions derived from regression analysis. These polynomial expressions are incorporated into the two-phase model to calculate fluidization parameters such as bubble diameter and velocity, which are involved in the deposition rate estimation. Then, the particle size distribution is determined using the population balance equations. The particle size distribution significantly affects the fluidization behavior of the system, leading to the recalculation of the fluidization conditions periodically using the polynomic expression.

The modeling approach developed by Dutta[56] provides a more detailed and comprehensive description of the gas-solid interaction in terms of heat and mass transfer between the emulsion and bubble phases and incorporating the effect of the bubble formation. Furthermore, their work considers a more accurate description of the formation of fines, solving the population balance through the methods of moments to estimate the amount of powder over time. Conversely, the proposed modified plug-flow reactor (PFR) model does not consider the assumption of these two phases and the effect of bubbles in the calculations. In addition, it considers that every fine particle has the same size (d_{pf}) over time. These assumptions can oversimplify the system physics, leading to a significant discrepancy in the model predictions. Therefore, these two models are compared to analyze the effect of these assumptions in the calculations. The initial conditions used for the comparison are summarized in Table 5.5.

5.3.1 Open-loop simulations

The dynamics described by each model are presented in Fig 5.9. In general, both modeling approaches showcase similar particle growth dynamics. Fig 5.9a corresponds to the evolution of the particle size distribution, indicating a notable discrepancy in the transient region

Table 5.5: *Modified plug-flow model vs Two-phase model: Initial Conditions.*

Parameter	**Value**	**Symbol**
Reactor height	6 m	h
Reactor diameter	0.3 m	D
Inlet gas velocity	0.55 m/s	v_{in}
Inlet Concentration - Silane	6.5 mol/m^3	$C_{\mathrm{SiH_4}}^{\mathrm{in}}$
Inlet Concentration - Hydrogen	26 mol/m^3	$C_{\mathrm{H_2}}^{\mathrm{in}}$
Inlet Concentration - Silicon Powder	0.001 mol/m^3	$C_{\mathrm{Si}}^{\mathrm{in}}$
Reaction Enthalpy	2000 J/mol	ΔH
Fine diameter	$0.3 \times 10^{-6} m$	d_{f}
Seed addition rate	0.001 mol/s	S
Initial Solid bed	350 kg	M
Mass hold-up	450 kg	M^*
Reaction Enthalpy	2000 J/mol	ΔH
Overall heat transfer coefficient	$150\ W/m^2K$	U
Reactor wall Temperature	900 K	T_r
Inlet gas Temperature	500 K	T

between both models. It is observed that the two-phase model exhibits a faster dynamic response compared to the modified PFR model. However, the mismatch between both models at steady-state conditions is minor ($0.05mm$). Fig 5.9b illustrates a similar dynamic behavior regarding the available surface area. This discrepancy in the dynamic response observed in Fig 5.9a and Fig 5.9b is principally caused by the deposition rate estimated by each model. Fig 5.9c presents the deposition rate calculated by each model, indicating a significant difference during the early simulation hours. In particular, the two-phase model predicts a higher deposition rate than the modified plug-flow model at the initial hours of operation, producing a faster particle growth dynamic in the initial stage. After a few hours, the deposition rate decreases over time, being more pronounced in the case of the two-phase model. This reduction mainly results from the depletion of the available surface area due to particle growth. After 50 hours, the deposition rate predicted by the two-phase model is lower compared to the modified PFR model, maintaining the same situation at steady-state conditions. The temperature distribution has a significant effect on the deposition rate. Fig 5.9e displays the temperature profiles corresponding to each model. In the case of the two-phase model, different temperature profiles are considered for the emulsion and bubble phases.

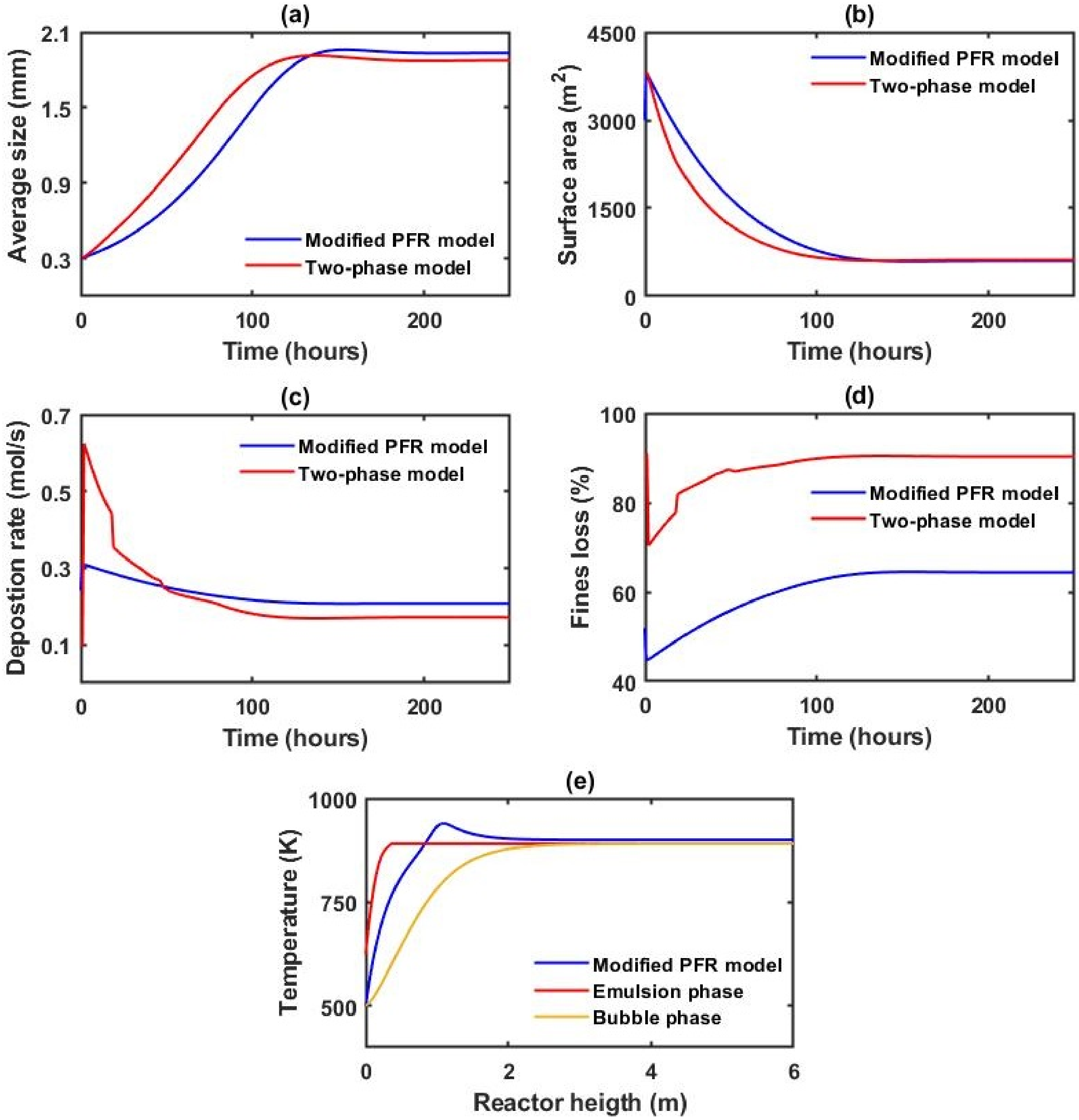

Figure 5.9: *Modified PFR model vs Two-phase model:(a) average particle size, (b) available surface area, (c) total deposition rate, and (d) powder loss, (e) temperature distribution.*

Despite both models considering the same reactor wall temperature and initial gas temperature, the temperature profile obtained from each model is different. This discrepancy causes a difference in the deposition rate estimated by each model. For instance, the two-phase model achieves higher temperatures in the emulsion region, producing a high silane conversion after a few centimeters from the entrance of the reactor. It produces large amounts of powder in the solid region (emulsion phase) due to the high temperatures, increasing the likelihood of the fine particles being scavenged by larger particles in the bed and contributing to achieving a larger estimated deposition rate value. This result is also noticeable in the powder loss generation. The powder loss estimated by both models is presented in Fig 5.9d, denoting a distinguished difference in the predictions performed by each model. A large fraction of powder loss is calculated by the two-phase model, suggesting a higher contribution of the homogeneous decomposition in the silane pyrolysis. In particular, homogeneous decomposition can simultaneously increase the powder loss and deposition rate via a scavenging mechanism. However, the scavenging factor determines the fraction of fines contributing to particle growth. Hence, a higher powder loss indicates a higher amount of fines produced via homogenous decomposition, which is favored in the emulsion phase due to the high temperatures.

Despite the noticeable difference in the transient region, both models generally show similar dynamic responses. In particular, the modified plug-flow model is suitable for capturing the dynamics of the FBR system compared with the two-phase model developed by Dutta[56], which is a more reliable representation of the actual system. Therefore, the proposed model can be utilized as a basis for control purposes using MPC.

5.3.2 Closed-loop Simulations

The prediction and control horizons are set to $N_p = N_c = 10$ sampling, with a sampling time of $\Delta = 5$ hours for each MPC iteration. Therefore, the prediction horizon for solving the optimal control problem at each sampling instance is determined as $T_p = T_c = 50$ hours. It is assumed that all states can be measured at every sampling time. Table 5.6 contains the desired steady-state conditions for stabilizing the system. The same conditions from the previous case studies for weight matrices, optimization algorithms, and constraints are considered in this case.

Table 5.6: *Case Study 4: Steady State Values.*

Parameter	Value	Symbol
Mass hold-up	450 kg	x_1^{SS}
Average Particle size	1.90 mm	x_2^{SS}
Seed addition rate	0.001 mol/s	u_1^{SS}
Inlet gas velocity	0.55 m/s	u_2^{SS}

5.3.3 Case Study 4

In this case, a mismatch between the process model and the actual system is considered using a nominal MPC. The modified plug-flow reactor is used as the process model for MPC calculations, while the two-phase model is used as the actual system. Hence, the controller must handle disturbances and uncertainties associated with the process model without additional robustness considerations. The results from the closed-loop simulation are presented in Fig 5.10

The seed addition rate and inlet gas velocity are shown in Fig 5.10a and Fig 5.10b, respectively. In this case, the controller converges gradually to the steady-state values after a few iterations, even considering the mismatch between both models. This indicates that the nominal MPC is inherently robust enough to handle this situation. The control actions reach a steady-state condition after 50 hours. The transient response of the mass hold-up (Fig. 5.10c) and the particle size distribution (Fig. 5.10d) converge with smooth trajectories to their steady-state values. Therefore, these results indicate that the nominal MPC can stabilize the system to its steady-state values, even considering the mismatch between the process model and the actual system. It is important to mention that the mismatch between both models is larger in the transient region, while this error is significantly smaller at the steady-state condition (Fig 5.9a). However, the discrepancy between these models can be larger under different parameters and operational conditions. The advantage of using a simplified representation of the actual system for MPC calculation is the reduced computa-

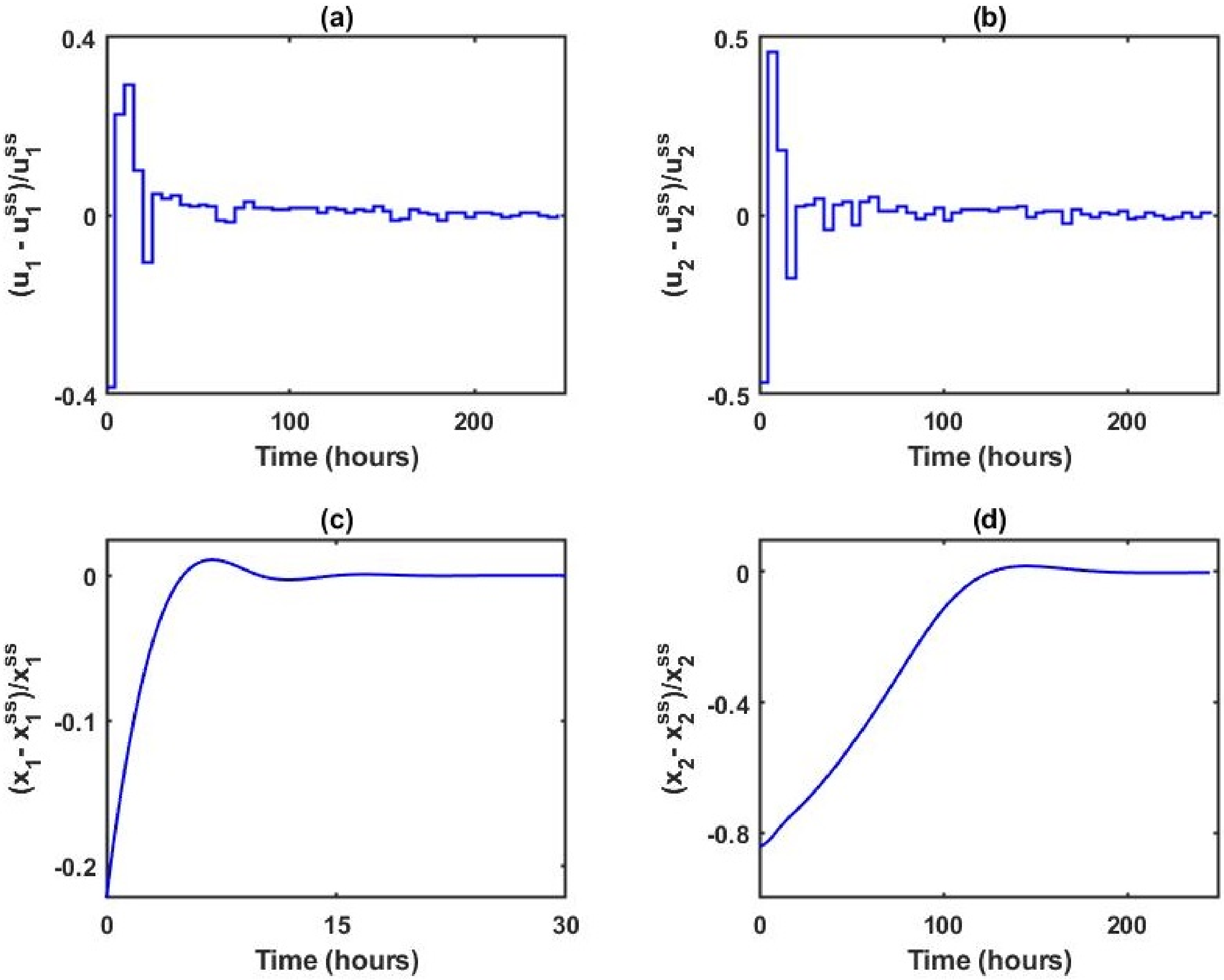

Figure 5.10: *Case Study 4 - Closed-loop system dynamics: (a) seed addition rate, (b) inlet gas velocity, (c) mass holdup, (d) average particle size.*

tional cost, allowing the controller to converge faster to the optimal solution. Furthermore, it reduces the complexity of the optimization problem. However, the nominal MPC can be susceptible to performing poorly against anomalous external disturbance or high uncertainty.

5.3.4 Case Study 5

In this case, implementing RMPC to handle the mismatch between the process model and the actual system is considered. This case presents a more realistic situation for the robust MPC implementation, where the process model provides a simplified representation of the actual system. Based on the open-loop simulation illustrated in Fig 5.11, their uncertainties could be related to the discrepancy in the deposition rate predicted by each model. The scavenging factor largely contributes to the uncertainty involved in the deposition calculation. Furthermore, estimating the scavenging factor depends on several operational conditions and fluctuates constantly during operation. However, in general, the reported models in the literature considered this parameter as a constant adjustable parameter determined by comparing model predictions with experimental data[3;20;31;56]. In this case, the RMPC considers an uncertainty within the range ±0.10% of the estimated scavenging factor in the process model. In the case of the two-phase model, this parameter remains a constant value ($k_{sc} = 0.03$). Fig 5.11 displays the closed-loop response of the system considering the mismatch in RMPC calculations.

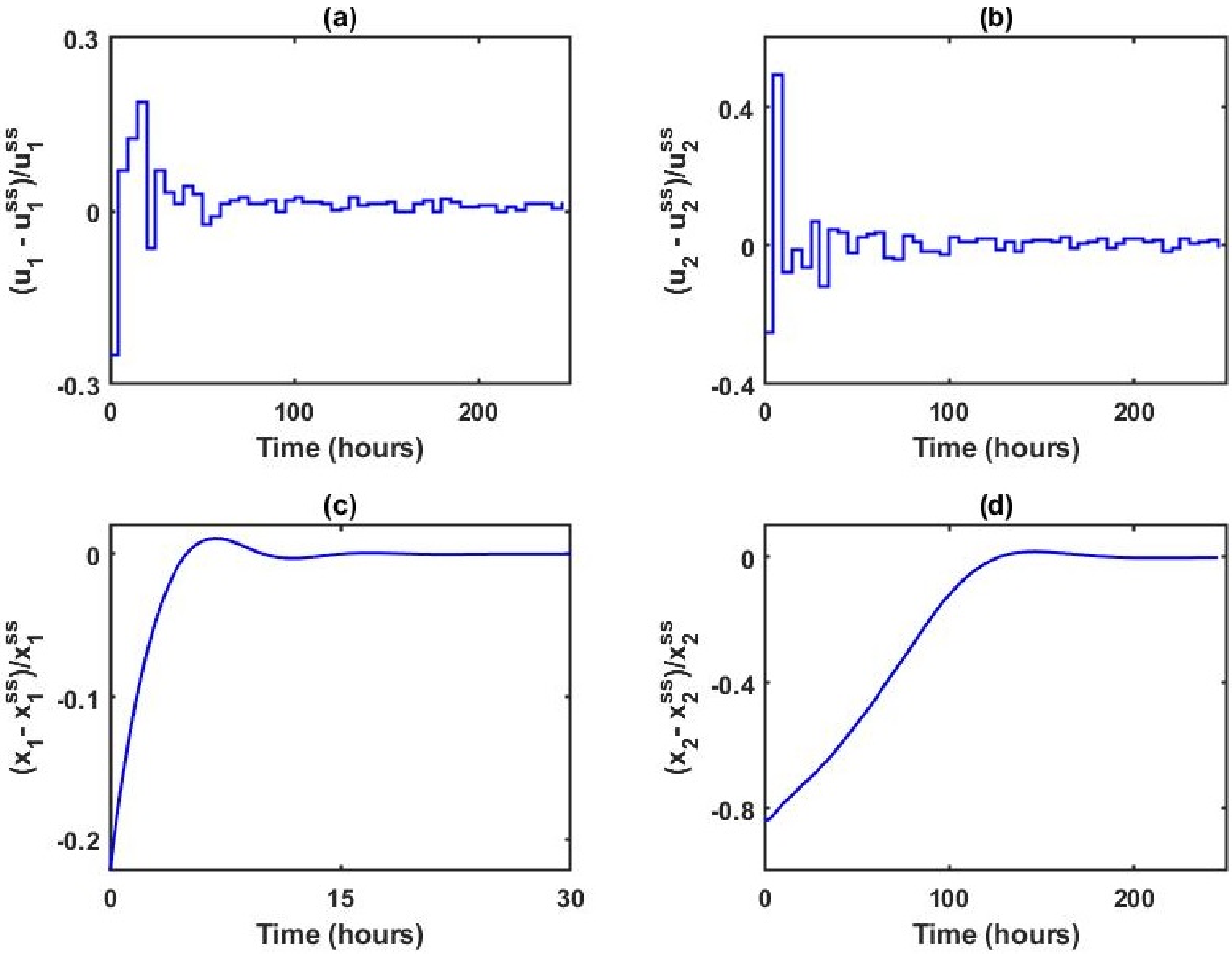

Figure 5.11: *Case Study 5 - Closed-loop system dynamics: (a) seed addition rate, (b) inlet gas velocity, (c) mass holdup, (d) average particle size.*

The dynamic behavior of the mass holdup (Fig. 5.11c) and the particle size distribution (Fig. 5.11d) displays an equivalent transient response to the previous case study. The seed addition rate and the inlet gas velocity are shown in Fig 5.11a and Fig 5.11b, respectively. In this case, the controller reaches the steady-state value following smoother and more gradual trajectories, even considering the mismatch in the RMPC calculations. In particular, RMPC determines more conservative control actions based on the worst scenario due to the bounded uncertainties included in the calculations. As a result, the deviation of the control action values with respect to their steady state values calculated by the RMPC is smaller compared to the results obtained using nominal MPC. For instance, the inlet gas velocity input computed by nominal MPC is bounded within ± 0.5, while using RMPC, this control action is bounded in a smaller range from -0.3 to 0.42. In real scenarios, working with less aggressive variations and fluctuations of the actuators or valves is favorable for preserving the equipment life use longer during operation. In general, the RMPC performs better in the presence of model mismatch because it explicitly incorporates the effect of uncertainties into the calculations.

Chapter 6

Conclusion and Outlook

This work presents a control-oriented predictive model for polysilicon production in FBR systems. Two modeling approaches with different flow regimes and assumptions are developed to analyze the dynamic behavior of the silane pyrolysis in fluidized-bed reactors. A well-mixed regime and a plug-flow regime are considered to describe the dynamics in the gas phase, concluding that the plug-flow model provides a better representation of the gas phase due to the incorporation of the concentration gradients along the reactor. The proposed model incorporates temperature and concentration gradients to describe the silane decomposition along the reactor and utilizes the population balance model to predict particle growth. Several open-loop simulations were performed to analyze the effect of the temperature distribution in the particle growth dynamics, concluding that reactor temperature has a significant impact on promoting silane decomposition via specific reaction pathways. Hence, regulating the reactor temperature is a crucial factor that can significantly improve the overall yield of the process. Finally, the developed model exhibited a satisfactory performance compared against a more comprehensive model reported in the literature.

The feasibility of integrating nonlinear MPC with the proposed model is validated through simulation results. Several case studies were analyzed, considering different modeling approaches. The results show the MPC's effectiveness in regulating mass hold-up and controlling the particle size distribution in the final product. Furthermore, the RMPC controller showcases a satisfactory performance considering a mismatch between the process model and the actual system for the calculations. Therefore, the proposed predictive modeling and control framework indicates a promising approach for developing more advanced control strategies used in the operation of particulate systems, especially for contributing to the enhancement of silicon production in fluidized systems. Improving the control strategies is essential to enhance polysilicon production in fluidized-bed systems. MPC strategy appears to be a promising approach due to the features and benefits regarding its functionality, robustness, and performance. Future research needs to develop more specific control strategies to minimize powder loss during FBR operation. In particular, Economic MPC represents a possible and feasible alternative to improve the overall yield from an economic perspective by reducing the powder loss and maximizing the profit benefit during operation.

Bibliography

[1] Kouji Yasuda, Kazuki Morita, and Toru H Okabe. Processes for production of solar-grade silicon using hydrogen reduction and/or thermal decomposition. *Energy Technology*, 2(2):141–154, 2014.

[2] H Scott Fogler. *Elements of chemical reaction engineering*. Pearson, 2020.

[3] S Balaji, Juan Du, CM White, and B Erik Ydstie. Multi-scale modeling and control of fluidized beds for the production of solar grade silicon. *Powder Technology*, 199(1): 23–31, 2010.

[4] Deren Yang. *Handbook of Photovoltaic Silicon*, volume 205. Springer, 2019.

[5] Daniel Simon. *Model Predictive Control in Flight Control Design - Stability and Reference Tracking*. PhD thesis, 03 2014.

[6] Limin Jiang, Benjamin F Fieselmann, Liguo Chen, and David Mixon. Fluidized bed process with silane. In *Handbook of Photovoltaic Silicon*, pages 69–108. Springer, 2019.

[7] Yuelong Yu, Xinjie Bai, Shaoyuan Li, Jianghao Shi, Lei Wang, Fengshuo Xi, Wenhui Ma, and Rong Deng. Review of silicon recovery in the photovoltaic industry. *Current Opinion in Green and Sustainable Chemistry*, page 100870, 2023.

[8] Christophe Ballif, Franz-Josef Haug, Mathieu Boccard, Pierre J Verlinden, and Giso Hahn. Status and perspectives of crystalline silicon photovoltaics in research and industry. *Nature Reviews Materials*, 7(8):597–616, 2022.

[9] Juan Du and BE Ydstie. Modeling and control of particulate processes and application to poly-silicon production. *Chemical Engineering Science*, 67(1):120–130, 2012.

[10] Shwetank Yadav, Kinnor Chattopadhyay, and Chandra Veer Singh. Solar grade silicon production: A review of kinetic, thermodynamic and fluid dynamics based continuum scale modeling. *Renewable and sustainable energy reviews*, 78:1288–1314, 2017.

[11] S Lai, PA Ramachandran, et al. Chemical vapor deposition and homogeneous nucleation in fluidized bed reactors: silicon from silane. *Chemical Engineering Science*, 41(4):633–641, 1986.

[12] B Caussat, M Hemati, and JP Couderc. Silicon deposition from silane or disilane in a fluidized bed—part ii: theoretical analysis and modeling. *Chemical engineering science*, 50(22):3625–3635, 1995.

[13] Loïc Cadoret, Nicolas Reuge, Sreekanth Pannala, Madhava Syamlal, Carole Coufort, and Brigitte Caussat. Silicon cvd on powders in fluidized bed: Experimental and multi-fluid eulerian modelling study. *Surface and Coatings Technology*, 201(22-23):8919–8923, 2007.

[14] George Hsu, Naresh Rohatgi, and John Houseman. Silicon particle growth in a fluidized-bed reactor. *AIChE journal*, 33(5):784–791, 1987.

[15] Kenji Hashimoto, Kouichi Miura, Takao Masuda, Masaaki Toma, Hiroyuki Sawai, and Motoaki Kawase. Growth kinetics of polycrystalline silicon from silane by thermal chemical vapor deposition method. *Journal of the Electrochemical Society*, 137(3):1000, 1990.

[16] Maria P Tejero-Ezpeleta, Sigurd Buchholz, and Leslaw Mleczko. Optimization of reaction conditions in a fluidized-bed for silane pyrolysis. *The Canadian Journal of Chemical Engineering*, 82(3):520–529, 2004.

[17] Dan Shi, Nael H El-Farra, Mingheng Li, Prashant Mhaskar, and Panagiotis D Christofides. Predictive control of particle size distribution in particulate processes. *Chemical Engineering Science*, 61(1):268–281, 2006.

[18] Doraiswami Ramkrishna. *Population balances: Theory and applications to particulate systems in engineering*. Elsevier, 2000.

[19] Alan Randolph. *Theory of particulate processes: analysis and techniques of continuous crystallization*. Elsevier, 2012.

[20] Christy M White, Paul Ege, and B Erik Ydstie. Size distribution modeling for fluidized bed solar-grade silicon production. *Powder technology*, 163(1-2):51–58, 2006.

[21] Alan W Weimer and David E Clough. Dynamics of particle size/conversion distributions in fluidized beds: application to char gasification. *Powder Technology*, 26(1):11–16, 1980.

[22] Michael J Hounslow. A discretized population balance for continuous systems at steady state. *AIChE journal*, 36(1):106–116, 1990.

[23] Charles David Immanuel and Francis Joseph Doyle Iii. Computationally efficient solution of population balance models incorporating nucleation, growth and coagulation: application to emulsion polymerization. *Chemical Engineering Science*, 58(16):3681–3698, 2003.

[24] Christy M White, Gerald Zeininger, Paul Ege, and B Erik Ydstie. Multi-scale modeling and constrained sensitivity analysis of particulate cvd systems. *CHEMICAL VAPOR DEPOSITION-WEINHEIM-*, 13(9):507, 2007.

[25] Daizo Kunii and Octave Levenspiel. Bubbling bed model. model for flow of gas through a fluidized bed. *Industrial & Engineering Chemistry Fundamentals*, 7(3):446–452, 1968.

[26] B Caussat, M Hemati, and JP Couderc. Silicon deposition from silane or disilane in a fluidized bed—part i: Experimental study. *Chemical Engineering Science*, 50(22): 3615–3624, 1995.

[27] T Kojima, T Kimura, and M Matsukata. Development of numerical model for reactions

in fluidized bed grid zone-application to chemical vapor deposition of polycrystalline silicon by monosilane pyrolysis. *Chemical engineering science*, 45(8):2527–2534, 1990.

[28] Juliana Piña, Verónica Bucalá, Noemí Susana Schbib, Paul Ege, and Hugo Ignacio de Lasa. Modeling a silicon cvd spouted bed pilot plant reactor. *International Journal of Chemical Reactor Engineering*, 4(1), 2006.

[29] C Guenther, T O'Brien, and M Syamlal. A numerical model of silane pyrolysis in a gas-solids fluidized bed. In *Proceedings of the International Conference on Multiphase Flow*. Citeseer, 2001.

[30] Nicolas Reuge, Loïc Cadoret, and Brigitte Caussat. Multifluid eulerian modelling of a silicon fluidized bed chemical vapor deposition process: Analysis of various kinetic models. *Chemical Engineering Journal*, 148(2-3):506–516, 2009.

[31] James M Parker. Validation of cfd model for polysilicon deposition and production of silicon fines in a silane deposition fbr. *International Journal of Chemical Reactor Engineering*, 9(1), 2011.

[32] Si-Si Liu and Wen-De Xiao. Numerical simulations of particle growth in a silicon-cvd fluidized bed reactor via a cfd–pbm coupled model. *Chemical Engineering Science*, 111: 112–125, 2014.

[33] Juan Du, Soham Dutta, and Birger Erik Ydstie. Modeling and control of solar-grade silicon production in a fluidized bed reactor. *AIChE Journal*, 60(5):1740–1751, 2014.

[34] S Ranjan, S Balaji, Rocco A Panella, and B Erik Ydstie. Silicon solar cell production. *Computers & Chemical Engineering*, 35(8):1439–1453, 2011.

[35] B Erik Ydstie and Juan Du. Producing poly-silicon from silane in a fluidized bed reactor. *Solar Cells—Silicon Wafer-Based Technologies*, 2011.

[36] WO Filtvedt, A Holt, PA Ramachandran, and MC Melaaen. Chemical vapor deposition of silicon from silane: Review of growth mechanisms and modeling/scaleup of fluidized bed reactors. *Solar energy materials and solar cells*, 107:188–200, 2012.

[37] G. del Coso, I. Tobías, C. Cañizo, and A. Luque. Temperature homogeneity of polysilicon rods in a siemens reactor. *Journal of Crystal Growth*, 299(1):165–170, 2007. ISSN 0022-0248. doi: https://doi.org/10.1016/j.jcrysgro.2006.12.004. URL `https://www.sciencedirect.com/science/article/pii/S0022024806015624`.

[38] J Moriyama. Production of high-purity silicon–an overview (ii). *Suiyokwai-Shi*, 20: 597–605, 1987.

[39] Huiming Yin, Mehdi Zadshir, and Frank Pao. 3 - solar cell manufacture and module packaging. In Huiming Yin, Mehdi Zadshir, and Frank Pao, editors, *Building Integrated Photovoltaic Thermal Systems*, pages 129–193. Academic Press, 2022. ISBN 978-0-12-821064-2. doi: https://doi.org/10.1016/B978-0-12-821064-2.00012-2. URL `https://www.sciencedirect.com/science/article/pii/B9780128210642000122`.

[40] Vladimir N Jarkin, Oleg A Kisarin, and Tatyana V Kritskaya. Methods of trichlorosilane synthesis for polycrystalline silicon production. part 2: Hydrochlorination and redistribution. *Modern Electronic Materials*, 7(2):33–43, 2021.

[41] Pei Zhai and Eric D Williams. Dynamic hybrid life cycle assessment of energy and carbon of multicrystalline silicon photovoltaic systems. *Environmental science & technology*, 44(20):7950–7955, 2010.

[42] Gøran Bye and Bruno Ceccaroli. Solar grade silicon: Technology status and industrial trends. *Solar Energy Materials and Solar Cells*, 130:634–646, 2014. ISSN 0927-0248. doi: https://doi.org/10.1016/j.solmat.2014.06.019. URL `https://www.sciencedirect.com/science/article/pii/S0927024814003286`.

[43] Ran Fu, Ted L James, and Michael Woodhouse. Economic measurements of polysilicon for the photovoltaic industry: market competition and manufacturing competitiveness. *IEEE Journal of Photovoltaics*, 5(2):515–524, 2015.

[44] WO Filtvedt, M Javidi, A Holt, MC Melaaen, E Marstein, H Tathgar, and PA Ramachandran. Development of fluidized bed reactors for silicon production. *Solar Energy Materials and Solar Cells*, 94(12):1980–1995, 2010.

[45] MM Dahl, A Bellou, DF Bahr, MG Norton, and EW Osborne. Microstructure and grain growth of polycrystalline silicon grown in fluidized bed reactors. *Journal of crystal growth*, 311(6):1496–1500, 2009.

[46] A Ramos, WO Filtvedt, Dag Lindholm, Palghat A Ramachandran, A Rodríguez, and C Del Cañizo. Deposition reactors for solar grade silicon: A comparative thermal analysis of a siemens reactor and a fluidized bed reactor. *Journal of Crystal Growth*, 431:1–9, 2015.

[47] Nong M Hwang. Deposition and simultaneous etching of si in the chemical vapor deposition (cvd) process: approach by the charged cluster model. *Journal of crystal growth*, 205(1-2):59–63, 1999.

[48] Achi Brandt. Multiscale scientific computation: Review 2001. *Multiscale and Multiresolution Methods: Theory and Applications*, pages 3–95, 2002.

[49] Caterina Gonçalves Philippsen, Antônio Cezar Faria Vilela, and Leandro Dalla Zen. Fluidized bed modeling applied to the analysis of processes: review and state of the art. *Journal of Materials Research and Technology*, 4(2):208–216, 2015. ISSN 2238-7854. doi: https://doi.org/10.1016/j.jmrt.2014.10.018. URL `https://www.sciencedirect.com/science/article/pii/S2238785414001070`.

[50] Wen ching Yang. Handbook of fluidization and fluid-particle systems. *China Particuology*, 1:137, 2003. URL `https://api.semanticscholar.org/CorpusID:98693930`.

[51] Daizo Kunii and Octave Levenspiel. *Fluidization engineering*. Butterworth-Heinemann, 1991.

[52] Derek Geldart. Types of gas fluidization. *Powder technology*, 7(5):285–292, 1973.

[53] Ananda K Praturi, R Lutwack, and G Hsu. Chemical vapor deposition of silicon from silane pyrolysis. In *Proceedings of the Sixth International Conference on Chemical Vapor Deposition, 1977*, volume 77, page 20. Electrochemical Society, 1977.

[54] S Mori and CY Wen. Estimation of bubble diameter in gaseous fluidized beds. *AIChE Journal*, 21(1):109–115, 1975.

[55] Yue Huang, Palghat A Ramachandran, and Milorad P Dudukovic. Fluidized bubbling bed reactor model for silane pyrolysis in solar grade silicon production. In *AIChE Annual Meeting, Salt Lake City, UT*, 2007.

[56] Soham Dutta. Multiscale modeling of fluidized bed reactor for production of polysilicon, 2011.

[57] S. Benyahia, M. Syamlal, and T.J. O'Brien. Summary of mfix equations 2012-1, January 2012. From URL `https://mfix.netl.doe.gov/documentation/MFIXEquations2012-1.pdf`.

[58] A Passalacqua, RO Fox, R Garg, and S Subramaniam. A fully coupled quadrature-based moment method for dilute to moderately dilute fluid–particle flows. *Chemical Engineering Science*, 65(7):2267–2283, 2010.

[59] Pongpawee Chanlaor, Sunun Limtrakul, Terdthai Vatanatham, and Palghat A Ramachandran. Modeling of chemical vapor deposition of silane for silicon production in a spouted bed via discrete element method coupled with eulerian model. *Industrial & Engineering Chemistry Research*, 57(36):12096–12112, 2018.

[60] Ya-Qing Zhuang, Xiao-Min Chen, Zheng-Hong Luo, and Jie Xiao. Cfd–dem modeling of gas–solid flow and catalytic mto reaction in a fluidized bed reactor. *Computers & chemical engineering*, 60:1–16, 2014.

[61] Guangkai Gu, Guoqiang Lv, Wenhui Ma, Shanlin Du, and Boqiang Fu. Numerical simulation of granular silicon growth and silicon fines formation process in polysilicon fluidized bed. *Particuology*, 87:74–86, 2024.

[62] Stephen P Walch and Christopher E Dateo. Thermal decomposition pathways and rates for silane, chlorosilane, dichlorosilane, and trichlorosilane. *The Journal of Physical Chemistry A*, 105(10):2015–2022, 2001.

[63] WAP Claassen and J Bloem. The nucleation of cvd silicon on sio2 and si3 n 4 substrates: I. the system at high temperatures. *Journal of the Electrochemical Society*, 127(1):194, 1980.

[64] Farid F Abraham. *Homogeneous nucleation theory*, volume 263. Elsevier, 1974.

[65] Carlyle S Herrick and David W Woodruff. The homogeneous nucleation of condensed silicon in the gaseous si-h-cl system. *Journal of the Electrochemical Society*, 131(10): 2417, 1984.

[66] Carl L Yaws, Larry L Dickens, R Lutwack, and George Hsu. Semiconductor industry silicon: Physical and thermodynamic properties. *Solid State Technology*, 24(1):87–92, 1981.

[67] Sheldon K Friedlander et al. *Smoke, dust, and haze*, volume 198. Oxford university press New York, 2000.

[68] SK Iya, RN Flagella, and FS DiPaolo. Heterogeneous decomposition of silane in a fixed bed reactor. *Journal of the Electrochemical Society*, 129(7):1531, 1982.

[69] Hugh M Hulburt and Stanley Katz. Some problems in particle technology: A statistical mechanical formulation. *Chemical engineering science*, 19(8):555–574, 1964.

[70] S Joe Qin and Thomas A Badgwell. A survey of industrial model predictive control technology. *Control engineering practice*, 11(7):733–764, 2003.

[71] Max Schwenzer, Muzaffer Ay, Thomas Bergs, and Dirk Abel. Review on model predictive control: An engineering perspective. *The International Journal of Advanced Manufacturing Technology*, 117(5):1327–1349, 2021.

[72] Alberto Bemporad. Model predictive control design: New trends and tools. In *Proceedings of the 45th IEEE Conference on Decision and Control*, pages 6678–6683. IEEE, 2006.

[73] E. F. Camacho and C. Bordons. *Introduction to Model Predictive Control*, pages 1–11. Springer London, London, 2007. ISBN 978-0-85729-398-5. doi: 10.1007/978-0-85729-398-5_1. URL https://doi.org/10.1007/978-0-85729-398-5_1.

[74] James B Rawlings. Tutorial overview of model predictive control. *IEEE control systems magazine*, 20(3):38–52, 2000.

[75] Daniel Limon, Teodoro Alamo, Davide M Raimondo, D Muñoz De La Peña, José Manuel Bravo, Antonio Ferramosca, and Eduardo F Camacho. Input-to-state stability: a unifying framework for robust model predictive control. *Nonlinear Model Predictive Control: Towards New Challenging Applications*, pages 1–26, 2009.

[76] James Blake Rawlings, David Q Mayne, and Moritz Diehl. *Model predictive control: theory, computation, and design*. Nob Hill Publishing Madison, WI, 2 edition, 2017.

[77] Eduardo F Camacho, Carlos Bordons, EF Camacho, and C Bordons. Nonlinear model predictive control. *Model predictive control*, pages 249–288, 2007.

[78] Frank Allgower, Rolf Findeisen, Zoltan K Nagy, et al. Nonlinear model predictive control: From theory to application. *Journal-Chinese Institute Of Chemical Engineers*, 35(3):299–316, 2004.

[79] David Q Mayne, James B Rawlings, Christopher V Rao, and Pierre OM Scokaert. Constrained model predictive control: Stability and optimality. *Automatica*, 36(6): 789–814, 2000.

[80] Davood Babaei Pourkargar, Ali Almansoori, and Prodromos Daoutidis. Impact of decomposition on distributed model predictive control: A process network case study. *Industrial & Engineering Chemistry Research*, 56(34):9606–9616, 2017.

[81] Rodrigo S Gesser, Daniel M Lima, and Julio E Normey-Rico. Robust model predictive control: Implementation issues with comparative analysis. *IFAC-PapersOnLine*, 51(25): 478–483, 2018.

[82] Pierre OM Scokaert and David Q Mayne. Min-max feedback model predictive control for constrained linear systems. *IEEE Transactions on Automatic control*, 43(8):1136–1142, 1998.

[83] Eric C Kerrigan and Jan M Maciejowski. Feedback min-max model predictive control using a single linear program: robust stability and the explicit solution. *International Journal of Robust and Nonlinear Control: IFAC-Affiliated Journal*, 14(4):395–413, 2004.

[84] David Mayne. Robust and stochastic model predictive control: Are we going in the right direction? *Annual Reviews in Control*, 41:184–192, 2016.

[85] Byron Tasseff, Carleton Coffrin, Andreas Wächter, and Carl Laird. Exploring benefits of linear solver parallelism on modern nonlinear optimization applications. *arXiv preprint arXiv:1909.08104*, 2019.

[86] Lorenz T Biegler. *Nonlinear programming: concepts, algorithms, and applications to chemical processes*. SIAM, 2010.

[87] S Se Zabrodsky. Heat transfer between solid particles and a gas in a non-uniformly aggregated fluidized bed. *International Journal of Heat and Mass Transfer*, 6(1):23–31, 1963.

[88] Matthew Ellis, Helen Durand, and Panagiotis D Christofides. A tutorial review of economic model predictive control methods. *Journal of Process Control*, 24(8):1156–1178, 2014.